Available online at www.sciencedirect.com
SCIENCE DIRECT®
Journal of Computational Physics 214 (2006) 366–396
JOURNAL OF COMPUTATIONAL PHYSICS
www.elsevier.com/locate/jcp

A front tracking method for a deformable intravascular bubble in a tube with soluble surfactant transport

J. Zhang [a], D.M. Eckmann [b], P.S. Ayyaswamy [a,*]

[a] *Department of Mechanical Engineering and Applied Mechanics, University of Pennsylvania, 229 Towne Building, 220 S. 33rd Street, Philadelphia, PA 19104, United States*
[b] *Department of Anesthesia, University of Pennsylvania, United States*

Received 6 August 2004; received in revised form 16 September 2005; accepted 26 September 2005
Available online 8 November 2005

Abstract

Based on a front tracking scheme, we have presented a comprehensive algorithm for the study of a deformable bubble moving in a tube in the presence of a soluble or an insoluble surfactant. The emphasis here is on the dynamic adsorption of the soluble surfactant which non-linearly alters the surface tension, and this in turns affects the flow and transport in a complicated way. Furthermore, since a bubble–liquid interface is being examined, there is a need to accommodate a concentration jump across the interface in the evaluation of flow and transport. Standard numerical procedures need to be modified to accommodate this feature. Based on the physics governing the problem, an axisymmetric formulation is found to be adequate and is thus considered. The adsorption scheme for the soluble surfactant is carefully designed such that the total mass of the surfactant is well conserved, and the mass flux is accurately resolved by using an interface indicator function. This represents an advance in treating problems of this class. Tests on the efficacy of various aspects of the algorithm have been carried out. The algorithm has the flexibility of studying different models for adsorption/desorption and surfactant surface tension models, such as the Langmuir and the Frumkin models. These models have significant practical relevance. The numerical results obtained are qualitatively consistent with results where available. The results presented include an example of Marangoni flow which causes a bubble to propel out of its initial static location due to the development of a surface tension gradient. It is also shown that the bubble motion in Poiseuille flow may be significantly slowed down due to the presence of a soluble surfactant in the bulk medium. In that case, the Marangoni induced motion is in a direction opposite to that driven by the bulk pressure. Our study indicates that as the location of the adsorptive interface gets closer to the tube wall, the bulk fluid in the vicinity of the interface may become depleted of surfactant, an observation that has particular significance in understanding gas embolism and for developing therapeutic measures.

Keywords: Bubble; Poiseuille flow; Insoluble surfactant; Soluble surfactant; Front tracking; Marangoni effects; Pulmonary embolism

* Corresponding author. Tel.: +1 2158988362; fax: +1 2155736334.
E-mail address: ayya@seas.upenn.edu (P.S. Ayyaswamy).

0021-9991/$ - see front matter © 2005 Elsevier Inc. All rights reserved.
doi:10.1016/j.jcp.2005.09.016

1. Introduction

Our goal here is to develop a general algorithm for computing the convection-diffusion transport of surface active agents (surfactants) from the bulk medium (continuous phase) contained in a tube onto the surface of a bubble in the medium (dispersed phase). We illustrate our method through the investigation of the behavior of a gas bubble immersed in an arteriolar blood vessel or micro vessel with liquid-phase soluble or insoluble surfactant. The soluble surfactant present in the liquid phase gets adsorbed onto or is desorbed from the gas–liquid interface. Simulating this complex system involves the detailed description of the interaction between bulk quantities and excessive surface quantities in terms of surfactant surface concentration and non-linear, composition dependent alteration of surface tension. Depending on the surface concentration of surfactant, this non-linear interaction affects the flow field and the shape/dynamics of the bubble in a complicated way.

This investigation has particular significance in the study of gas embolism, a common syndrome for surgery and decompression sickness. Gas bubbles may enter the blood stream during cardiopulmonary bypass for cardiac operations or in vascular procedures. This may also happen due to decompression from hyperbaric exposures, such as in diving or extravehicular activity during space exploration. The intravascular gas emboli may deposit into organs, like the heart or the brain, and as a result, cause permanent injury. Surfactant based intervention [2,14] is a novel treatment to eliminate such risks, and the present study will enable an evaluation of this process. A suitable, soluble, inert surfactant introduced into the system may adsorb onto the gas–liquid interface and may modify the interfacial tension, and also shield biological moieties in the blood stream from encountering an adsorptive surface. Our investigation has significance also in the study of activation of blood clotting, initiation of inflammation, and testing with biochemical reaction in a multiphase flow regime.

In regard to existing literature relevant to the problem, the motion of a clean bubble in a tube containing a Newtonian or a non-Newtonian fluid has been extensively studied. Some recent contributions in this area include those of Cavanagh and Eckmann [5] on stationary gas bubbles in Newtonian flows in an inclined tube and Tsai and Miksis [42] study on the dynamics of a drop in a constricted capillary fluid filled tube using a boundary integral method. Sussman and Puckett [39] have described a coupled level set/volume-of-fluid (CLSVOF) method and have, among other examples, demonstrated the capability of the method to compute the steady rise of an axisymmetric gas bubble rising in a viscous liquid with a density ratio is 714:1 and a viscosity ratio of 6667:1. The far-field boundary condition, i.e., the pressure on the walls is prescribed to be $p = z/Fr$, where Fr is the Froude number. This method is stated to be more accurate than either the level set or volume-of-fluid method alone especially, when computing problems for which the surface tension and the changes in the topology of the free surface are dominant features of the flow. Sussman [40] has employed CLSVOF method to compute the growth and collapse of vapor bubbles to overall second order accuracy. The discretization of the free surface pressure boundary condition is based on the method described by Gibou et al. [19] for solving the Poisson equation, and this feature enables the enforcement of the boundary condition to second order accuracy. A comprehensive review of the experimental and theoretical results on a bubble moving in an infinite non-Newtonian fluid is presented by Chhabra [8,9], and De Kee and Chhabra [11]. Bubble shape in non-Newtonian fluids has been studied by De Kee, Chan Man Fong and Yao [12]. Their results indicate the possibility of cusp formation at the rear end of the bubble. Rodrigue [34,35] has proposed a generalized correlation for gas bubbles rising in both uncontaminated viscous Newtonian and power-law fluids.

The presence of a surfactant in the medium makes the bubble problem very much more complicated. The effects of insoluble surfactants on drop deformation and breakup in extension flow have been investigated by Stone [38]. Since the surfactant is assumed to be insoluble, there is no net mass transport between the bulk phase and the interface. A boundary integral method has been applied to solve for the velocity. Jan and Tryggvason [21] have presented a computational procedure based on the front tracking method for investigating the behavior of a bubble contaminated by an insoluble surfactant. Tsai and Miksis [43] have extended their earlier work on clean bubbles to take into account the effects of an insoluble surfactant on the dynamics of bubble snap-off. In fully 3-D simulations, Li and Pozrikidis [25] and Yon and Pozrikidis [48] have studied various cases of drop deformation in the presence of an insoluble surfactant in the limit of Stokes flow. They have employed the boundary integral method. Eggleton, Pawar and Stebe [15] have investigated the effect of the non-linear equation of state for a drop in an extension flow with an insoluble surfactant. Eggleton, Tsai and Stebe [16] have studied the onset of tip streaming in presence of insoluble surfactants.

In regard to the presence of a soluble surfactant, analytical results have been obtained for a few simplified cases. Oğuz and Sadhal [30] have used a matched asymptotic analysis to study the effects of a soluble surfactant on the motion of drops. The low Reynolds number flow is associated with a steady stagnant cap model on a spherical drop [37]. Park [31] has investigated the steady motion of a long inviscid bubble displacing a viscous fluid under the influence of a soluble surfactant in the Stokes flow regime using an asymptotic approach. The result obtained is able to explain the film thickening behavior at low Ca that is observed in experiments. Soluble surfactant effects have been considered in the Stokes flow limit by Milliken and Leal [28] for an axisymmetric drop, and recently by Zhou et al. [49] for describing 3-D drop–drop interactions and coalescence. In [49], a finite element method has been proposed to solve drop interactions and coalescence problems in the presence of a soluble surfactant, in the Stokes regime. It is unclear how well the mass conservation for the soluble surfactant has been satisfied in that study. Ghadiali and Gaver [17] have demonstrated the influence of non-equilibrium surfactant dynamics on the flow of a semi-infinite bubble in Stokes regime. Rodrigue, De Kee and Chan Man Fong [36] have investigated the slow motion of a single gas bubble rising in a contaminated fluid described by power-law or three parameter Carreau models. Their analysis shows the balance between shear thinning and Marangoni effects.

Recent numerical simulations of the behavior of a drop in the presence of a surfactant have involved conformal mapping, volume-of-fluid, and level set methods. A finite-volume based numerical approach has been employed by Leppinen, Renksizbulut and Haywood [24] to solve the coupled set of governing equations for a situation involving an insoluble surfactant. The algorithm employs non-orthogonal grid generation. Cuenot, Magnaudet and Spennato [10] have numerically investigated the effects of a soluble surfactant on the flow around a spherical bubble. They have treated the bubble as a void and solved the formulation using orthogonal curvilinear coordinates. The shape of the drop has been assumed to remain spherical throughout this simulation. Liao and McLaughlin [27] have simulated the effects of a surfactant on the unsteady motion and shape of a single bubble released in water. They have considered the bubble to be immersed in an unbounded liquid medium and have also treated the bubble as a void. A time-dependent mapping method is utilized in this study. Even though it is stated that a "void bubble" is not a constraining feature for the mapping method, it may be noted that a detailed numerical study of the dispersed and continuous phases within a confined tube would be considerably more complicated with this method. Li and Mao [26] have used an approach similar to that of Liao and McLaughlin [27]. Ghadiali, Halpern and Gaver [18] have shown that a dual-reciprocity boundary element method can be utilized to evaluate bulk convective transport of a soluble surfactant in a steady Stokes flow with a free surface.

Renardy and co-workers [13,33] have employed the volume-of-fluid method, assuming a linear relation between the surfactant concentration and surface tension. James and Lowengrub [20] have proposed a surfactant-conserving volume-of-fluid scheme for interfacial flows with an insoluble surfactant. Ceniceros [6] has used a hybrid level-set and front tracking method to study the surfactant effects on capillary waves. Xu and Zhao [47] present a methodology to simulate surfactant transport on a deformable interface using the level set method. However, satisfying mass conservation in this procedure is of concern. Takemura [41] has investigated the adsorption of a surfactant onto the surface of a spherical rising bubble by solving the Navier–Stokes equation and the convection-diffusion equations of the surfactants in the bulk and on the surface at steady state. The numerical procedure involves the upwind scheme and the SOR method.

We note that there are significant difficulties in generalizing the above numerical techniques to simulate the unsteady motion of a deformable bubble under the influence of a soluble surfactant in the low and moderate Reynolds number regimes. In particular, since our study described here involves flows beyond the Stokes regime, boundary element and dual-reciprocity boundary element methods cannot be employed. In the present study, we have developed a comprehensive algorithm based on the front tracking method for solving the formulation.

The front tracking method for the numerical study of flow systems described by Unverdi and Tryggvason [44,45] explicitly introduces a separate interfacial grid in addition to the fixed regular Marker and Cell (MAC) grid. This has proven to be an effective and robust numerical method to describe surface related phenomena, for example, dendritic growth, boiling, bubbly flow [3,4,22,23]. On this basis, in the present study, we propose a suitably modified front tracking scheme to address the problem of mass transport between the deformable moving bubble surface and surfactant quantities in the bulk medium. We note that our algorithm deals with

species transport from the liquid phase onto a bubble interface during adsorption and desorption from the interface into the liquid phase. Since the bubble phase is devoid of external species, the algorithm must accommodate a concentration jump at the interface. This treatment is fundamentally different from those of many earlier studies, for example, the mass transfer in solidification considered in [22,44] and drop interactions with a soluble surfactant considered in [49], where the transformed concentration is continuous at the interface. Thus, the numerical techniques used in discretizing the surface term such as those described in [22,44] cannot be directly employed here. New techniques for tracking the one-sided interfacial flux and discretization of the surface integral terms are noteworthy features of the present study. The algorithm conserves the total amount of surfactant very well. The details are provided in later sections.

2. Problem formulation

In a blood vessel, the core flow may be represented as non-Newtonian while the flow near the vessel wall boundary mainly consists of blood plasma which may be considered Newtonian. Here, for simplicity, we shall treat the entire continuous phase (bulk) fluid medium as blood plasma (Newtonian). Although this is a drastic simplification, the knowledge gained by addressing this problem is invaluable to make progress on the more realistic coupled formulation involving non-Newtonian and Newtonian fluid flow in a vessel containing an insoluble or a soluble surfactant together with the presence of a bubble.

We emphasize that we are motivated to develop a numerical method to evaluate the behavior of gas embolism bubbles. Since bubble lodging occurs when bubble diameter is of the same order magnitude as the diameter of the blood vessel, into which it progresses [2,14], the asymmetry is often small and can be ignored. Thus, it is sufficient to set up the problem in an axisymmetric geometry, as shown in Fig. 1.

We assume that there are two viscous, immiscible and incompressible fluids, labeled $j = 1, 2$, in a circular tube. Their densities and viscosities are denoted by ρ_j and $\mu_j, j = 1, 2$, respectively. Fluid 2 consists of a gaseous bubble dispersed in bulk fluid 1. The bubble is initially spherical and is of radius r_0 and volume $V = (4\pi/3)r_0^3$. The two fluids are separated by an interface with surface tension, σ, which varies with surfactant concentration on the interface, Γ (mol/cm^2). There is soluble surfactant transport from the bulk phase (fluid 1) on to the

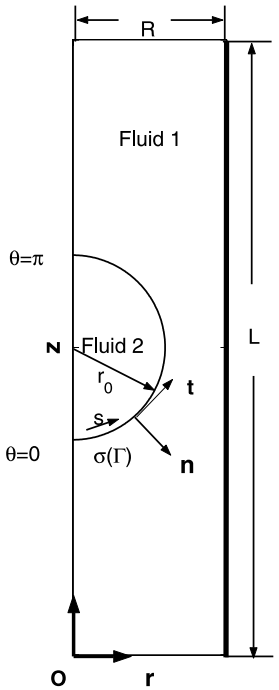

Fig. 1. Configuration of a bubble flow in a tube.

bubble–fluid interface. The radius of the tube is R. The tube length is unrestricted; however, for computational simplicity, herein we will consider segments of tube of length L and we seek a spatially periodic solution with periodicity L in the z direction (see Fig. 1). Each tube segment of length L is assumed to contain a bubble. We will include investigations for various values of L to ascertain the "best" L. The origin of the cylindrical coordinate (r,z) is set at the bottom-left corner of the domain, which is on the axis of symmetry of the tube.

The motion of the continuous and dispersed phases are governed by continuity and incompressible Navier–Stokes equations [44]. Further, the soluble surfactant is adsorbed on the gas–liquid interface from the bulk phase (liquid), and there may be desorption. It is assumed that the surfactant exists on the interface as a monolayer. The surface motion of the surfactant is governed by a convection-diffusion equation together with an interfacial adsorption/desorption source term in the case of a soluble surfactant. As stated earlier, an important feature of the problem is the presence of a gas–liquid interface. The concentration of the surfactant in the gas phase is negligible. This leads to a consideration of a concentration jump at the interface.

In terms of variables ρ, μ and diffusion coefficient D, we write,

$$\rho(r,z,t) = \rho_2 H(r,z,t) + \rho_1(1 - H(r,z,t)), \tag{1}$$

$$\mu(r,z,t) = \mu_2 H(r,z,t) + \mu_1(1 - H(r,z,t)) \tag{2}$$

and

$$D = D_1(1 - H(r,z,t)). \tag{3}$$

Here, D_1 is the diffusion coefficient for the surfactant in bulk phase (fluid 1), t is time, and $H(r,z,t)$ is a Heaviside function such that,

$$H(r,z,t) = \begin{cases} 1 & (r,z,t) \text{ in fluid 2,} \\ 0 & (r,z,t) \text{ in fluid 1.} \end{cases}$$

Following [44,38], the governing equations become:

$$\frac{\partial \rho \mathbf{u}}{\partial t} + \nabla \cdot \rho \mathbf{u}\mathbf{u} = -\nabla p + \nabla \cdot \mu(\nabla \mathbf{u} + \nabla^{\mathrm{T}}\mathbf{u}) + \int_S \left[\sigma(\Gamma(s))\kappa' \mathbf{n}' + \frac{\partial \sigma(\Gamma(s))}{\partial s}\mathbf{t}'\right]\delta(\mathbf{x} - \mathbf{x}')\,\mathrm{d}S', \tag{4}$$

$$\frac{\partial C}{\partial t} + (\mathbf{u} \cdot \nabla)C = \nabla \cdot (D \nabla C) - \int_S \left[k_{\mathrm{a}} C_{\mathrm{S}}\left(1 - \frac{\Gamma}{\Gamma_\infty}\right) - k_{\mathrm{d}}\Gamma \exp\left(-A\frac{\Gamma}{\Gamma_\infty}\right)\right]\delta(\mathbf{x} - \mathbf{x}')\,\mathrm{d}S', \tag{5}$$

and

$$\frac{\partial \rho}{\partial t} + \nabla \cdot (\mathbf{u}\rho) = 0. \tag{6}$$

In the above, $\mathbf{u}$ is the velocity, p is pressure, s is a measure of arc length from the bubble pole (see Fig. 1), S denotes the surface of the interface. Also, κ is the mean curvature of the surface, $\mathbf{n}$ is the outward normal vector on the interface pointing into bulk fluid 1, and $\mathbf{t}$ is the tangential vector; C is the molar concentration in the bulk (mol/cm^3), C_{S} is the concentration in the sublayer (mol/cm^3) adjacent to the interface, k_{a} is the coefficient of adsorption (cm/s), and k_{d} is the desorption coefficient (s^{-1}), ranging from 10^{-4} to 1 and 10^{-4} to 10^6, respectively. A is a prescribed interaction parameter for the Frumkin isotherm. When $A = 0$, the surface is ideal, and the Frumkin isotherm reduces to the Langmuir isotherm. Γ_∞ is the maximum monolayer surface concentration for the surfactant, and δ denotes the Dirac delta function. The sublayer is assumed to be very thin.

The periodicity condition for velocity in the z direction requires

$$\mathbf{u}(r,0,t) = \mathbf{u}(r,L,t), \tag{7}$$

for $0 \leqslant r \leqslant R$. The no-slip condition at the wall of the tube is described by

$$\mathbf{u}(R,z,t) = \mathbf{0}, \tag{8}$$

for $0 \leqslant z \leqslant L$, and from the assumption of axial symmetry,

$$\frac{\partial \mathbf{u}}{\partial r}(0,z,t) = \mathbf{0}. \tag{9}$$

The boundary condition for the bulk surfactant concentration C is also periodic in z and is given by

$$C(r,0,t) = C(r,L,t), \tag{10}$$

for $0 \leqslant r \leqslant R$. The no flux condition across the vessel wall $r = R$ implies,

$$\frac{\partial C}{\partial r}(R,z,t) = 0, \tag{11}$$

for $0 \leqslant z \leqslant L$, and from the symmetry assumption,

$$\frac{\partial C}{\partial r}(0,z,t) = 0. \tag{12}$$

Along the interface, the surface concentration of surfactant Γ is governed by a surface conservation equation of the adsorbed surfactant (see derivation by Stone [38])

$$\frac{\partial \Gamma}{\partial t} + \nabla_s \cdot (\mathbf{u}_s \Gamma) + \Gamma(\nabla_s \cdot \hat{\mathbf{n}})(\mathbf{u} \cdot \hat{\mathbf{n}}) = D_s \nabla_s^2 \Gamma + j_n, \tag{13}$$

where j_n, the diffusional flux and is given by Fick's law, $j_n = D_1(\hat{\mathbf{n}} \cdot \nabla)C$, with D_S for the surface diffusion coefficient. On the interface, the flux of surfactant is balanced via adsorption/desorption, given by

$$k_a C_S\left(1 - \frac{\Gamma}{\Gamma_\infty}\right) - k_d \Gamma \exp\left(-A\frac{\Gamma}{\Gamma_\infty}\right) = D_1(\hat{\mathbf{n}} \cdot \nabla)C. \tag{14}$$

This is implied by the surface integral term in Eq. (5). Surface tension $\sigma(\Gamma(s))$ is assumed to be governed by the Frumkin model

$$\sigma = \sigma_0 + RT\Gamma_\infty\left[\ln\left(1 - \frac{\Gamma}{\Gamma_\infty}\right) + \frac{A}{2}\left(\frac{\Gamma}{\Gamma_\infty}\right)^2\right], \tag{15}$$

where A is a prescribed interaction parameter in this evaluation, σ_0 is the surface tension for a clean surface, R is the gas constant, T is absolute temperature, and Γ_∞, as stated earlier, is the maximum monolayer surface concentration for surfactant. When $A = 0$, it reduces to the Langmuir equation of state

$$\sigma = \sigma_0 + RT\Gamma_\infty \ln\left(1 - \frac{\Gamma}{\Gamma_\infty}\right). \tag{16}$$

Initially, the spherical bubble is assumed to be in a laminar Poiseuille flow; thus,

$$\begin{cases} u(r,z,0) = 0, \\ v(r,z,0) = \frac{G}{4\mu_1}(1 - r^2), \end{cases} \tag{17}$$

where u and v denote the r and z component of flow velocity, G denotes the pressure gradient applied in the z direction. The surfactant concentration is assumed to be uniform in the bulk liquid phase.

$$C(r,z,0) = C_0(1 - H(r,z,0)), \tag{18}$$

where C_0 is the initial bulk concentration.

3. Non-dimensionalization of quantities

We introduce the following scheme for non-dimensionalization:

$$s = Rs^*, \quad r = Rr^*, \quad z = Rz^*, \quad \mathbf{u} = U_{\max}\mathbf{u}^*, \quad t = R/U_{\max}t^*, \tag{19}$$

$$p = \mu U_{\max}/Rp^*, \quad \sigma = \sigma_0\sigma^*, \quad C = C_0C^*, \quad \Gamma = \Gamma_\infty\Gamma^*, \tag{20}$$

where C_0 is the initial bulk concentration, $U_{\max} = G/(4\mu_1)$. Here, $*$ denotes dimensionless quantities. With this scheme, the dimensionless equations become

$$Re\left(\frac{\partial \rho^* \mathbf{u}^*}{\partial t^*} + \nabla \cdot \rho^* \mathbf{u}^* \mathbf{u}^*\right) = -\nabla p^* + \nabla \cdot \mu^* (\nabla \mathbf{u}^* + \nabla^{\mathrm{T}} \mathbf{u}^*) + \frac{1}{Ca} \int_S \left[\sigma^* \kappa \mathbf{n}' + \frac{\partial \sigma^*}{\partial s} \mathbf{t}'\right] \delta(\mathbf{x} - \mathbf{x}') \, \mathrm{d}S', \tag{21}$$

$$\frac{\partial C^*}{\partial t^*} + (\mathbf{u}^* \cdot \nabla) C^* = Pe^{-1} \nabla \cdot (D^* \nabla C^*) - \int_S [St_{\mathrm{a}} C_{\mathrm{s}}^* (1 - \Gamma^*) - \lambda St_{\mathrm{d}} \Gamma^* \exp(-A\Gamma^*)] \delta(\mathbf{x} - \mathbf{x}') \, \mathrm{d}S', \tag{22}$$

$$\frac{\partial \rho^*}{\partial t^*} + \nabla \cdot (\mathbf{u}^* \rho^*) = 0, \tag{23}$$

and

$$\frac{\partial \Gamma^*}{\partial t^*} + \nabla_{\mathrm{s}}^* \cdot (\mathbf{u}_{\mathbf{s}}^* \Gamma^*) = -\Gamma^* (\nabla_{\mathrm{s}}^* \cdot \hat{\mathbf{n}})(\mathbf{u}^* \cdot \hat{\mathbf{n}}) + Pe_{\mathrm{s}}^{-1} \nabla_{\mathrm{s}}^2 \Gamma^* + j^{*n}, \tag{24}$$

where $j^{*n} = (St_{\mathrm{a}}/\lambda) C_{\mathrm{s}}^* (1 - \Gamma^*) - St_{\mathrm{d}} \Gamma^* \exp(-A\Gamma^*)$, $\rho^* = \rho/\rho_1$, $\mu^* = \mu/\mu_1$ and $D^* = D/D_1$.

We note that there are eight dimensionless parameters involved: the Reynolds number, Re, the Capillary number, Ca, the bulk Peclect number, Pe, the surface Peclect number, Pe_{s}, the adsorption Stanton number, St_{a}, the desorption Stanton number, St_{d}, and the dimensionless adsorption depth, λ. They are defined by

$$\begin{aligned} &Re = \rho_1 U_{\max} R/\mu_1, \quad Ca = \mu_1 U_{\max}/\sigma_0, \quad Pe = U_{\max} R/D_1, \quad Pe_{\mathrm{s}} = U_{\max} R/D_{\mathrm{s}}, \\ &St_{\mathrm{a}} = k_{\mathrm{a}}/U_{\max}, \quad St_{\mathrm{d}} = k_{\mathrm{d}} R/U_{\max}, \quad \text{and} \quad \lambda = \Gamma_\infty/(C_0 R). \end{aligned} \tag{25}$$

The dimensionless surface tension σ^* is related to the dimensionless surface concentration Γ^* through

$$\sigma^* = 1 + El \ln(1 - \Gamma^*) \tag{26}$$

for the Langmuir model, and

$$\sigma^* = 1 + El \left[\ln(1 - \Gamma^*) + \frac{A}{2} \Gamma^{*2}\right] \tag{27}$$

for the Frumkin model, where the elasticity number $El = RT\Gamma_\infty/\sigma_0$. The non-dimensional boundary conditions for the velocities and concentration (7)–(12) will retain the same form as before but will now be starred quantities. We will omit superscript stars in subsequent writing for simplicity.

4. Numerical method

We need to solve the system (21)–(24). In these equations, the surface tension σ is a function of the surface concentration of the surfactant, Γ, which is affected both by the flow field and the adsorption/desorption process. Since the soluble surfactant can be adsorbed from the liquid phase onto the interface and desorbed from the interface to the bulk, the mass transfer needs to be accurately resolved in the neighborhood of the interface, and this is defined by an interface indicator function. We note that there is a concentration jump at the interface, since the gas medium has negligible concentration of the surfactant. The presence and extent of surfactant at the interface changes the surface tension gradient, and this in turn affects the flow field and transport. As a consequence, the instantaneous conservation of mass of the surfactant in the system becomes a very important feature in the algorithm. For this purpose, we employ a conservative discretization scheme for the flow field description, and details are provided in a later section. The scheme for the Navier–Stokes solver used here is similar to that employed by Almgren et al. [1]. Since we need to solve the surface convection-diffusion equation along the interface of the bubble, the location of the interface forms part of the solution. The front tracking technique gives us the advantage of explicitly representing the interface, thus numerically enabling to describe the surface derivatives in (24) at each time step. To evaluate the surface integral, we have followed the procedure of Peskin [32]. A brief outline of our algorithm follows.

4.1. Basic algorithm

All the bulk state variables (velocity, pressure, density, viscosity, bulk concentration) are defined at the center of each regular fixed cell in the computational domain, and all the interfacial state variables (surface tension, surface concentration) are defined on a time dependent movable interfacial grid as in [44]. The time

centered forcing terms are computed to maintain the second order of accuracy for the discretization scheme. At each time step, the interfacial grid is moved with the local velocity. This ensures that the velocity boundary conditions are satisfied. The movement of the interfacial grid is described by

$$\mathbf{x}_{\mathrm{f}}^{n+1} = \mathbf{x}_{\mathrm{f}}^{n} + \mathbf{u}_{\mathrm{f}}^{n}\Delta t, \tag{28}$$

where $\mathbf{x}_{\mathrm{f}}^{n}$ is the current interfacial grid location, and $\mathbf{u}_{\mathrm{f}}^{n}$ is its local velocity which is obtained by a linear interpolation of the velocity values at the nearest neighbors. The basic algorithm consists of the following:

1. Solve the coupled equation system (21)–(23) using a predictor–corrector method. First, proceed with the predictor step.
2. Move the interface at time step n to time step $n+\frac{1}{2}$, and evaluate the corresponding interface indicator function.
3. Solve (24) to get the values of $\Gamma^{n+\frac{1}{2}}(s)$.
4. Use Eq. (26) or (27) to evaluate $\sigma^{n+\frac{1}{2}}(s)$, then calculate the time centered integral terms in (21).
5. Calculate the time centered integral terms in (22) by using $\Gamma^{n+\frac{1}{2}}(s)$.
6. Proceed to the corrector step to get the intermediate velocity, and project it onto a divergence free vector space.
7. Proceed to the corrector step to get the bulk concentration at the $(n+1)$th step.
8. Solve (24) to get the intermediate values of $\Gamma^{n+1}(s)$.
9. Update the location of the interface and evaluate the corresponding interface indicator function at the $(n+1)$th time.

More detailed descriptions of each of these operations are given in the following sections.

4.2. Use of the Navier–Stokes solver for Eqs. (21)–(23)

We note that Almgren et al.'s [1] method may be extended to an adaptive mesh. This would be particularly advantageous for the investigation of the motion of a big bubble in a tube where the gas–liquid interface is very near the vessel wall and the bubble almost occludes the tube.

A projection method is applied to solve Eqs. (21)–(23). First, we solve the advection-diffusion equations (21)–(23) to get the updated density and concentration, and then we compute the intermediate velocity field. These are given by,

$$\frac{\hat{\mathbf{u}}-\mathbf{u}^{n}}{\Delta t} = -[\nabla\cdot(\mathbf{u}\mathbf{u})]^{n+\frac{1}{2}} + \frac{1}{Re\rho^{n+\frac{1}{2}}}\left\{-\nabla p^{n-\frac{1}{2}} \quad + \frac{1}{2}[\nabla\cdot\mu^{n}(\nabla\mathbf{u}^{\mathbf{n}} + \nabla^{\mathrm{T}}\mathbf{u}^{\mathbf{n}}) + \nabla\cdot\mu^{n+1}(\nabla\hat{\mathbf{u}} + \nabla^{\mathrm{T}}\hat{\mathbf{u}})] + \frac{1}{Ca}H_{u}^{n+\frac{1}{2}}\right\}, \tag{29}$$

$$\frac{C^{n+1}-C^{n}}{\Delta t} = -[\nabla\cdot(\mathbf{u}C)]^{n+\frac{1}{2}} + H_{C}^{n+\frac{1}{2}} + \frac{1}{2Pe}[\nabla\cdot D^{n}(\nabla C^{n} + \nabla^{\mathrm{T}}C^{n}) + \nabla\cdot D^{n+1}(\nabla C^{n+1} + \nabla^{\mathrm{T}}C^{n+1})], \tag{30}$$

$$\frac{\rho^{n+1}-\rho^{n}}{\Delta t} = -[\nabla\cdot(\rho\mathbf{u})]^{n+\frac{1}{2}}, \tag{31}$$

where $\wedge$ on $\mathbf{u}$ denotes intermediate value, and $H_{u}^{n+\frac{1}{2}}$ and $H_{C}^{n+\frac{1}{2}}$ are the integral source terms in Eqs. (21) and (22). To evaluate the diffusion term in Eq. (30), a central difference scheme is utilized for all cells except for those that are within one mesh size and adjacent to the interface. For cells adjacent to the interface, special treatment is needed to ensure that the flux boundary condition (14) is identically satisfied. The detailed implementation is addressed in the following section. An unsplit second order upwind predictor–corrector scheme is applied for evaluating the advective terms. The upwind method is an explicit difference scheme which has a time step restriction for numerical stability. Here, this restriction is expressed as (see Minion [29]):

$$\Delta t \leqslant \frac{1}{2}\min\left(\min\left(\frac{\Delta r}{u},\frac{\Delta z}{v}\right), \min\left(\sqrt{\frac{2\Delta r}{|H_{u}-(\nabla p)|/Re}}\right)\right). \tag{32}$$

Following the evaluation of advection-diffusion terms, we project this intermediate field onto the space of a vector field which approximately satisfies the divergence free constraint. In particular, **P**, the projection operator, is given by

$$\frac{\mathbf{u}^{n+1}-\mathbf{u}^{n}}{\Delta t}=\mathbf{P}\left(\frac{\hat{\mathbf{u}}-\mathbf{u}^{n}}{\Delta t}\right), \tag{33}$$

$$\frac{1}{\rho^{n+\frac{1}{2}}}\nabla p^{n+\frac{1}{2}}=\frac{1}{\rho^{n+\frac{1}{2}}}\nabla p^{n-\frac{1}{2}}+(\mathbf{I}-\mathbf{P})\left(\frac{\hat{\mathbf{u}}-\mathbf{u}^{n}}{\Delta t}\right). \tag{34}$$

The projection operator is computed discretely by solving the Poisson equation

$$\nabla\cdot\left(\frac{1}{\rho^{n+\frac{1}{2}}}\nabla\phi\right)=\nabla\cdot\left(\frac{\hat{\mathbf{u}}-\mathbf{u}^{n}}{\Delta t}\right), \tag{35}$$

and updating the velocity and pressure at the new time step by

$$\frac{\mathbf{u}^{n+1}-\mathbf{u}^{n}}{\Delta t}=\left(\frac{\hat{\mathbf{u}}-\mathbf{u}^{n}}{\Delta t}\right)-\frac{1}{\rho^{n+\frac{1}{2}}}\nabla_h\phi, \tag{36}$$

$$p^{n+\frac{1}{2}}=p^{n-\frac{1}{2}}+\phi. \tag{37}$$

In the above, ϕ is the pressure correction term.

4.2.1. Interface indicator function

In Eq. (30), the surface integral term, $H_C^{n+\frac{1}{2}}$, denoting surfactant adsorption is discretized on the background fixed grid. It is important to note that H_C has non-zero value only in the partial neighborhood of the interface in the liquid phase. Also, it is noted that a central difference scheme to evaluate the diffusion term is valid only for cells located away from the interface. For cells close to the interface, special treatment is needed to ensure that the boundary condition (14), which is represented as an integral source term in Eq. (30), holds true. A convenient way to locate these cells is to use an interface indicator function, which is defined at the cell center, as follows:

$$I_{i,j}(r_i,z_j)=\begin{cases}1, & (r_i,z_j)\text{ in fluid 1, interface does not pass through cell }(i,j),\\ 0.5, & (r_i,z_j)\text{ in fluid 1, interface passes through cell }(i,j),\\ -0.5, & (r_i,z_j)\text{ in fluid 2, interface passes through cell }(i,j),\\ -1, & (r_i,z_j)\text{ in fluid 2, interface does not pass through cell }(i,j).\end{cases} \tag{38}$$

This indicator function possesses unique features for identifying certain cells. An illustration of the two-dimensional grid structure and value of indicator function is shown in Fig. 2(a). One can identify which phase the cell is in simply from the sign of the indicator function $I_{i,j}$, and determine whether the cell is in the neighborhood of the interface simply from the magnitude of $I_{i,j}$. If $|I_{i,j}|=0.5$, then we call such cell as interfacial cell. The averaged value of $I_{i,j}$s on a finer mesh is its value on a coarser mesh. This unique feature can provide much programming convenience in using a multigrid solver to solve (30).

If the cell center (r_i,z_j) is located away from the interface, i.e., both the cell and its neighbors are all in a single phase with no interface passing through, then the diffusion term can be evaluated by central difference. However, if either the cell (i,j) or at least one of its immediate neighbors $(i\pm1,j\pm1)$ is an interfacial cell, then one needs to use the flux value in calculating the divergence instead of employing the central difference scheme. A simple example in one dimension is illustrated in Fig. 2(b). The ith cell is the interfacial cell, where $\frac{\partial C}{\partial x}=F_i$ on the interface I. F_i is the mass flux from liquid phase onto the interface. Cell $i+1$ is in the liquid phase, and cell $i-1$ is in the gas phase. The second order approximation of the Laplacian value at $i+1$ is

$$\left(\frac{\partial^2 C}{\partial x^2}\right)_{i+1}=\frac{\left(\frac{\partial C}{\partial x}\right)_{i+\frac{3}{2}}-\left(\frac{\partial C}{\partial x}\right)_{i+\frac{1}{2}}}{h}, \tag{39}$$

where

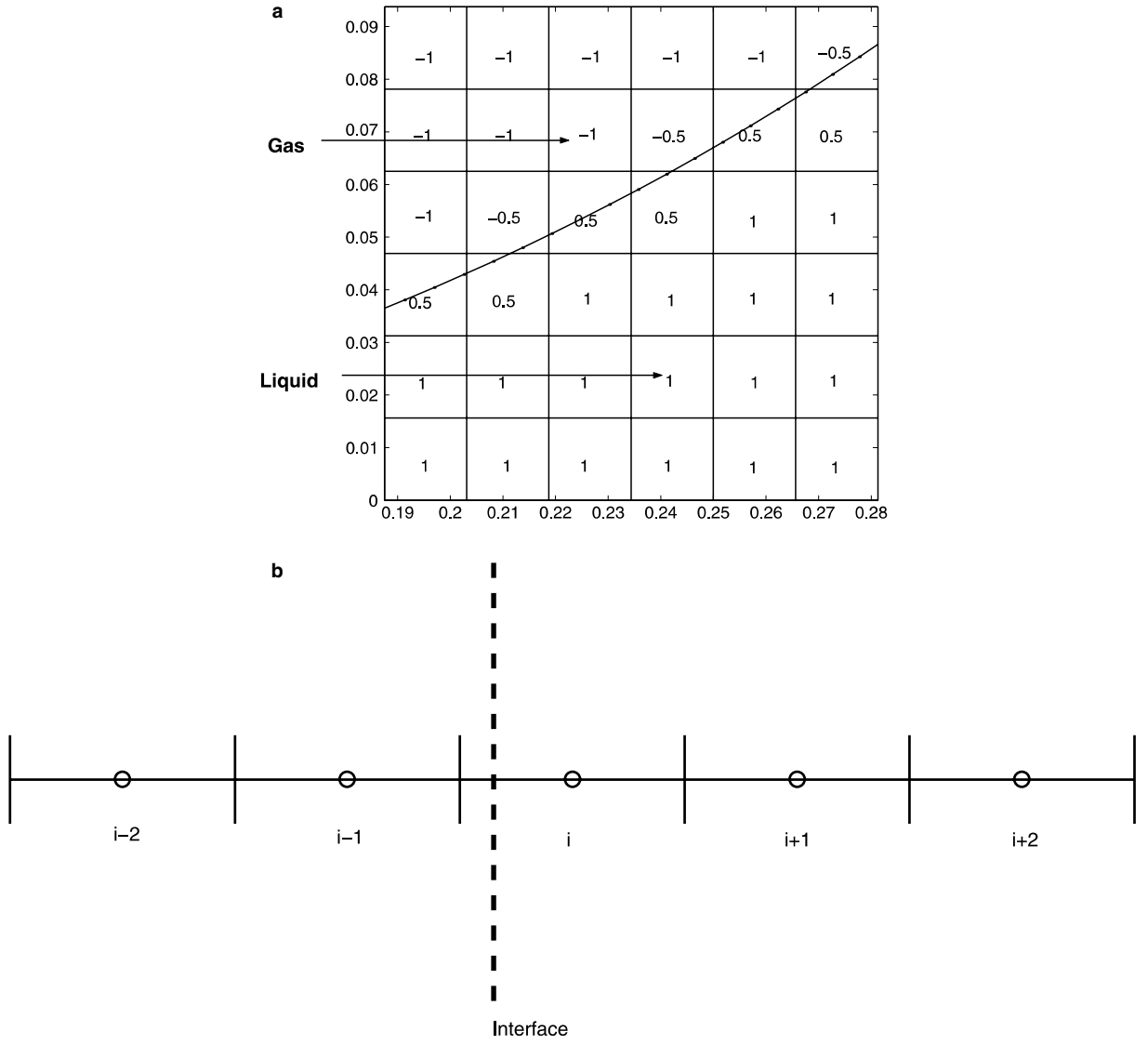

Fig. 2. Mesh and interfacial grid: (a) two dimensions, (b) one dimension.

$$\left(\frac{\partial C}{\partial x}\right)_{i+\frac{1}{2}} = F_i, \tag{40}$$

$$\left(\frac{\partial C}{\partial x}\right)_{i+\frac{3}{2}} = \frac{C_{i+2} - C_{i+1}}{h}. \tag{41}$$

To compute the Laplacian at $i-1$, we use $\left(\frac{\partial C}{\partial x}\right)_{i-\frac{1}{2}} = 0$.

For a two-dimensional problem, the horizontal and vertical fluxes of the interfacial cell are defined as the projected values of ∇C in the horizontal and vertical direction, respectively. Thus,

$$\frac{\partial C}{\partial x_k} = \nabla C \cdot \mathbf{n}_k, \tag{42}$$

where $\mathbf{n}_k = \mathbf{n} \cdot \hat{k}$, and $\hat{k}$ is the kth unit vector.

4.2.2. Discretization of surface integral term

To compute the surface integral terms, $H_u^{n+\frac{1}{2}}$ and $H_C^{n+\frac{1}{2}}$, in Eqs. (29) and (30), numerical interfacial integration is needed. Since the interface between the two fluids is explicitly tracked by the additional grid, the surface integral term can be easily evaluated. This surface quantity is distributed to the regular MAC grid by multiplication with a delta function which is here approximated by a delta sequence function with a finite support. Since the mass transport of soluble surfactant only occurs in the liquid phase, the surface integral in the bulk concentration Eq. (30) requires special care.

For the surface tension term in Eq. (29), $H_u^{n+\frac{1}{2}}$ is given by

$$\begin{aligned} H_u^{n+\frac{1}{2}} &= \left[\int_S \left(\sigma(\Gamma(s))\kappa'\mathbf{n}' + \frac{\partial\sigma}{\partial s}\mathbf{t}'\right)\delta(\mathbf{x}-\mathbf{x}')\,\mathrm{d}S'\right]^{n+\frac{1}{2}} \\ &\approx \sum_i \int_{S_i^{n+\frac{1}{2}}} \left(\sigma\left(\Gamma\left(s_i^{n+\frac{1}{2}}\right)\right)\kappa_i'\mathbf{n}_i' + \frac{\partial\sigma^{n+\frac{1}{2}}}{\partial s}\mathbf{t}_i'\right)\delta_{1,h}(\mathbf{x}-\mathbf{x}')\,\mathrm{d}S_i^{n+\frac{1}{2}}, \end{aligned} \tag{43}$$

where $\delta_{1,h}$ is a delta sequence function defined by

$$\delta_{1,h}(r,z) = \begin{cases} \frac{1}{4h^2}\left(1+\cos\left(\frac{\pi}{h}r\right)\right)\left(1+\cos\left(\frac{\pi}{h}z\right)\right), & |r|<h \quad \text{and} \quad |z|<h, \\ 0, & \text{otherwise}, \end{cases} \tag{44}$$

and i denotes a surface element. Here, h denotes the mesh size; $\mathbf{n}$ and $\mathbf{t}$ are calculated using a spline fit through the locations of the interfacial grid. Following [44], we find the tangents through a Legendre polynomial fit. For an axi-symmetric setup, following Weatherburn [46], it can be shown that $\kappa\mathbf{n} = -\mathbf{i_r}/r + \partial\mathbf{t}/\partial s$. Thus, we have,

$$\int_{S_i} \sigma\kappa\mathbf{n}\,\mathrm{d}s = \sigma\int_{S_i}\left(-\frac{\mathbf{i_r}}{r}+\frac{\partial\mathbf{t}}{\partial s}\right)\mathrm{d}s \approx \sigma\left[(\mathbf{t_2}-\mathbf{t_1}) - s_i\frac{\mathbf{i_r}}{r}\right], \tag{45}$$

where s_i is the arc length of the ith element S_i. Therefore, instead of finding the curvature, we only need to find the tangent at the end points. The normal can now be calculated.

For each segment of the surface $S_i^{n+\frac{1}{2}}$, knowing the value of $\Gamma^{n+\frac{1}{2}}$, $\sigma^{n+\frac{1}{2}}$ may be computed through

$$\sigma^{n+\frac{1}{2}} = 1 + El\ln\left(1-\Gamma^{n+\frac{1}{2}}\right) \tag{46}$$

for the Langmuir isotherm, or

$$\sigma^{n+\frac{1}{2}} = 1 + El\left[\ln\left(1-\Gamma^{n+\frac{1}{2}}\right) + \frac{A}{2}\Gamma^{n+\frac{1}{2}2}\right] \tag{47}$$

for the Frumkin isotherm. The details on computing this integration term follow the procedure described by Unverdi and Tryggvason [44,45].

Next, to compute the surface integral term, H_C^n in Eq. (30), we note that

$$\begin{aligned} H_C^n &= \left[\int_S (St_a C_s(1-\Gamma) - \lambda St_d\Gamma\exp(-A\Gamma))\delta(\mathbf{x}-\mathbf{x}')\,\mathrm{d}S'\right]^n \\ &\approx \sum_i \int_{S_i^{n+\frac{1}{2}}} \left(St_a C_s(1-\Gamma_i^*) - \lambda St_d\Gamma_i\exp(-A\Gamma_i)\right)\delta_{2,h}(\mathbf{x}-\mathbf{x}')\,\mathrm{d}S_i^n. \end{aligned} \tag{48}$$

Note that in Eq. (30), surfactant can only be depleted from the bulk phase (fluid 1). If the standard delta function discretization, which has support on both sides of the interface, were to be applied, then the concentration of surfactant inside the bubble would become non-physical (negative). This is displayed in Fig. 3. Thus, we need to construct a new discretized delta function $\delta_{i,+}$, whose support is only in the bulk phase (liquid). This is defined as follows:

$$\delta_{i,+}(r,z) = \begin{cases} 2\delta_{i,h}(r,z), & |r|<h, |z|<h \quad \text{and} \quad (r,z) \text{ in fluid 1}, \\ 0, & \text{otherwise}. \end{cases} \tag{49}$$

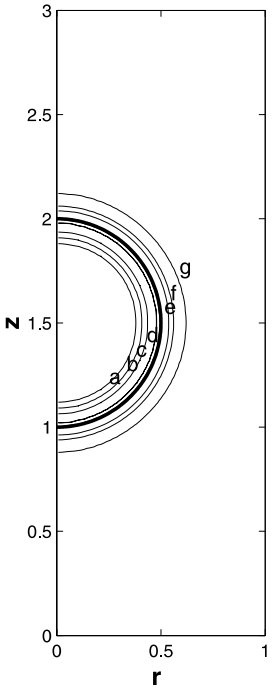

Fig. 3. Adsorption of an initially clean bubble in a tube with delta function $\delta_{1,h}$. Bubble interface is the thicker line. Bulk concentration contour at $t = 2$, (a) -0.001 (innermost contour), (b) -0.01, (c) -0.05, (d) -0.01, (e) 0.7, (f) 0.9, (g) 0.999 (outermost contour). $r_0 = 0.5$.

where $i = 1,2,3$; $\delta_{i,h}(r,z)$ is a regularly discretized delta function with a support on both sides of the interface. It is shown in Appendix A that for a simple one-dimensional case, the above function represents a delta sequence function, and has the same distribution as the delta function. However, in two dimensions, a numerical integration of this delta sequence function does not yield the exact value of unity as would be expected. In this context, we have tested three different forms of discretization of the delta function, $\delta_{1,+}(r,z)$, $\delta_{2,+}(r,z)$ and $\delta_{3,+}(r,z)$, in order to ascertain the "best" representation in the process of computing H_C^n. Thus,

$$\delta_{1,+}(r,z) = \begin{cases} \frac{2}{mh^2}\left(1-\frac{|r|}{h}\right)\left(1-\frac{|z|}{h}\right) & |r|<h, |z|<h, \quad \text{and} \quad (r,z) \quad \text{in} \quad \text{fluid 1}, \\ 0, & \text{otherwise}. \end{cases} \tag{50}$$

$$\delta_{2,+}(r,z) = \begin{cases} \frac{2}{4h^2}\left(1+\cos\left(\frac{\pi}{h}r\right)\right)\left(1+\cos\left(\frac{\pi}{h}z\right)\right) & |r|<h, |z|<h, \quad \text{and} \quad (r,z) \text{ in fluid 1}, \\ 0, & \text{otherwise}. \end{cases} \tag{51}$$

$$\delta_{3,+}(r,z) = \begin{cases} 2\left(\frac{3-4|\frac{r}{h}|+\sqrt{1+8|\frac{r}{h}|-16|\frac{r}{h}|^2}}{8}\right)\left(\frac{3-4|\frac{z}{h}|+\sqrt{1+8|\frac{z}{h}|-16|\frac{z}{h}|^2}}{8}\right) & |r|<h, |z|<h, \quad \text{and} \quad (r,z) \text{ in fluid 1}, \\ 0, & \text{otherwise}. \end{cases} \tag{52}$$

The "best" choice of δ will enable a very good satisfaction of the mass conservation requirement. Fig. 4 shows a measure for the mass conservation, $(M_t - M_e)/M_s$, as a function of dimensionless time t. Here, M_t is the total amount of surfactant in the system at any given instant (bulk plus surface), M_e is the total amount of surfactant initially in the system (only bulk quantity, no surface) at time $t = 0$, and is a prescribed quantity, while M_s is the total amount of surfactant on the surface at the given instant. As seen in Fig. 4, the "error" expressed as a percentage of surface concentration is about 1% when $\delta_{3,+}$ is employed. This choice of delta function discretization is noted to out-perform the other two choices. We will employ this $\delta_{3,+}$ in all of the evaluations. This procedure is a modification of the standard front tracking procedure.

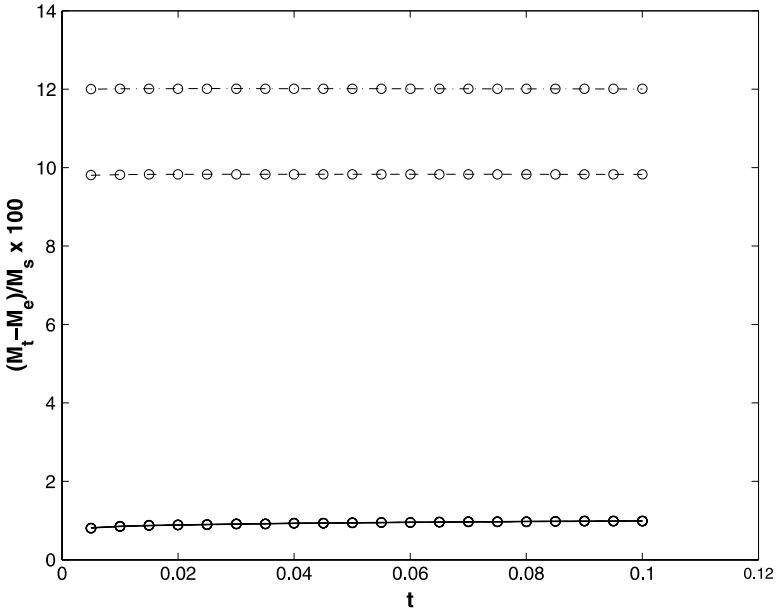

Fig. 4. Total mass error as a percentage of surface concentration for $\delta_{1,+}(r,z)$, -·-·-; $\delta_{2,+}(r,z)$, – – –; and $\delta_{3,+}(r,z)$, ——.

4.2.3. Discretization of the initial condition

The discretization of Eq. (18) requires some careful thought. In principle, for a fixed grid (r_i,z_j) (cell center), $C_{(i,j)}$ may be set equal to zero when (r_i,z_j) is inside the bubble surface, and equal to C_0 otherwise, (in the liquid phase). However, this provides a non-smooth, stepwise transition. With such a description, the concentration contours will not be sufficiently accurately determined, and in particular, the innermost ones will appear jagged. In the present study, a more accurate discretization of the concentration in each cell through which the interface traverses is implemented. Instead of a stepwise transition, the initial bulk concentration at the cell center is set equal to the product of the volume fraction of the cell with C_0. Here, the volume fraction is defined as the ratio of the volume of that portion of the cell which is in the liquid phase to the total volume of the cell (portion in liquid phase plus portion in gas phase). Thus, the contours are accurately evaluated.

4.3. Transfer between the bulk and the surface

To solve the surface convection-diffusion equation (24), we use a fourth order Runge–Kutta explicit time discretization. Thus,

$$\Gamma^{n+1} = \Gamma^n + \frac{\Delta t}{6}(k_1 + 2k_2 + 2k_3 + k_4), \tag{53}$$

where

$$k_1 = f(\Gamma^n, t^n), \tag{54}$$

$$k_2 = f\left(\Gamma^n + \frac{k_1}{2}, t^n + \frac{\Delta t}{2}\right), \tag{55}$$

$$k_3 = f\left(\Gamma^n + \frac{k_2}{2}, t^n + \frac{\Delta t}{2}\right), \tag{56}$$

$$k_4 = f(\Gamma^n + k_3, t^n + \Delta t), \tag{57}$$

and

$$f(\Gamma(t), t) = -\nabla_{h_s} \cdot (\mathbf{u}_s(t)\Gamma(t)) - \Gamma(t)(\nabla_{h_s} \cdot \hat{\mathbf{n}})(\mathbf{u}_s \cdot \hat{\mathbf{n}}) + Pe_s^{-1}\nabla_{h_s}^2\Gamma(t) + j^n. \tag{58}$$

Here, $j'' = (St_a/\lambda)C_s(1-\Gamma)-St_d\Gamma\exp(-A\Gamma)$, u_s is the time dependent surface velocity, $\Gamma(t)$ is the time dependent and spatially varying surface concentration, and C_s is the bulk concentration in the thin sublayer. The quantity, $\mathbf{u}_s(t)$, is calculated as projection of the interfacial velocity in the tangential direction. We note that we are employing the Langmuir and the Frumkin isotherms. With the Frumkin isotherm, there is a non-linear term as noted from the left hand side of Eq. (14). The time step, Δt for the Frumkin isotherm case will therefore be different from that for the Langmuir case since the time step has to satisfy the stability criterion in either case. Physically, C_s is a constant in the sublayer in a direction normal to the interface, but will vary in the θ direction.

The thickness of the sublayer is assumed to be much smaller than the mesh size, and we only know the value of C at the centers of the grids in the vicinity of the interface. Therefore, we need an extrapolation scheme to evaluate C_S at any location in the sublayer, in particular at any given location on the outer boundary of the sublayer which is away from the bubble interface. Once this is determined, since the value of C_s at any point on the sublayer boundary is a constant in a direction normal to it, we can infer the value of C_i at the corresponding point on the interface by setting $C_i = C_s$ for the corresponding point. In the algorithm, the value of C_s is extrapolated from the bulk concentration values at nearby Euclidean points which are located in fluid 1 (see Fig. 5). Specifically, for each interfacial grid point of interest, labeled O in Fig. 5, we can locate its four closest Euclidean fixed background points. For example, if there are two closest points in the bulk fluid 1, such as C and D in Fig. 5(a), and if $|CO| = r_1$, and $|DO| = r_2$, then,

$$C_i = C_s|_O = \frac{C_C r_2 + C_D r_1}{r_1 + r_2}. \tag{59}$$

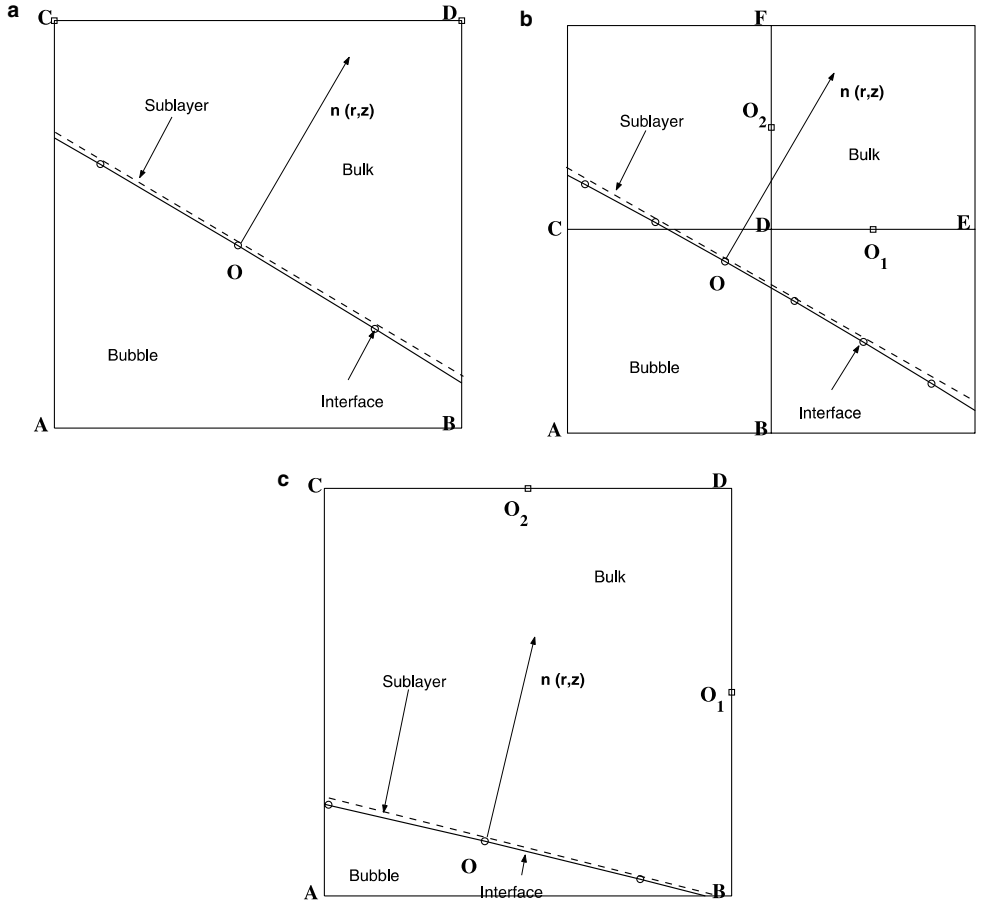

Fig. 5. Extrapolation of sublayer values on the interface.

To use the above extrapolation scheme consistently, there are two additional cases which have to be considered. These are shown in Fig. 5(b) and (c). If among its four closest fixed grid points, there is only one point in the bulk fluid 1, as illustrated in Fig. 5(b), we compute values at point O_1 and O_2 as the average value of D and E, and D and F, respectively. Then we invoke the previous description and may use O_1 and O_2, as in Eq. (59). Here, E and F are fixed grid points one mesh size away from D in the same direction as outer normal components. If there are three closest fixed grid points in the bulk fluid 1, as illustrated in Fig. 5(c), we compute values at point O_1 and O_2 which are the average values of B and D, and C and D, respectively. As before, we can use these values to compute $C_s|_O$ from Eq. (59). In this manner, we determine the instantaneous concentration value on the interface.

Next, note that $j^n = (St_a/\lambda)C_s(1-\Gamma) - St_d\Gamma\exp(-A\Gamma)$ in Eq. (58) is the sourcing term of the bulk concentration equation. Also, the total amount of mass transfer implied in Eq. (22) should be the same as that given by the surface integration of source term j^{*n} in the surface equation (24). This may be noted from the following:

$$\begin{aligned}
&\int_V \int_S [(St_a/\lambda)C_s(1-\Gamma) - St_d\Gamma\exp(-A\Gamma)]\delta(\mathbf{x}-\mathbf{x}')\,dS'\,dV \\
&\quad = \int_S \int_V [(St_a/\lambda)C_s(1-\Gamma) - St_d\Gamma\exp(-A\Gamma)]\delta(\mathbf{x}-\mathbf{x}')\,dV\,dS' \\
&\quad = \int_S [(St_a/\lambda)C_s(1-\Gamma) - St_d\Gamma\exp(-A\Gamma)]\,dS, \qquad (60)
\end{aligned}$$

where V is a thin shell that contains the interface S. In the numerical evaluation of these quantities, there will be a small error in mass conservation based on the choice of the delta function representation in the procedure. However, employing the $\delta_{3,+}$, the total mass of surfactant is sufficiently well conserved and this is noted in results discussed in a later section. We note that the quantity of surfactant taken from the bulk phase is limited by availability of the local amount of the surfactant, and the value of C physically can never become negative. Thus, at the center of a cell located adjacent to the interface but inside the bubble, we need to satisfy

$$-\hat{\mathbf{n}}\cdot\nabla C|_{\text{gas}} = 0 \text{ (flux free)} \qquad (61)$$

while $-\hat{\mathbf{n}}\cdot\nabla C|_{\text{liquid}}$ at the center of a cell located adjacent to the interface but in the liquid phase is given by Eq. (14). This treatment ensures that C never becomes negative.

5. Results and discussion

We examine a bubble moving in a cylindrical tube subject to a pressure driven flow field, in the presence of either a soluble or an insoluble surfactant. The parameters for computation are taken to be $R = 1$ cm, $L = 3$ cm, $\rho_1 = 1$ g/cm^3, $\rho_2 = 0.1$ g/cm^3, $\mu_1 = 0.01$ g/(cm s), and $\mu_2 = 0.01$ g/(cm s). Although ρ_2 chosen here does not correspond to a gas bubble, the $(\mu_1\rho_2)/(\mu_2\rho_1)$ value is representative of the typical kinematic viscosity ratio for an air bubble presence in the blood plasma. With this understanding, the dispersed phase will henceforth be called a bubble for simplicity. The dimensionless initial radius of the clean bubble is taken to be $r_0 = 0.5$ or $r_0 = 0.9$. The range of parameters investigated correspond to $Re = 1$, 10, based on tube radius, and $Ca = 0.01$. The computational results shown here employ a dimensionless mesh size (scaled with R) of $h = 2^{-6}$, and the reason for this choice is explained in a later section. In the following, unless stated otherwise, the Langmuir isotherm is employed.

First, we describe a number of tests to justify the choice of our computational domain corresponding to $L = 3$, and the mesh size, $h = 2^{-6}$, chosen in this numerical study.

5.1. Computational domain study

We first consider the case where $Re = 10$ and $Ca = 0.01$. The mesh size is set at $h = 2^{-6}$, and the density ratio, $\rho_2/\rho_1 = 0.1$. For these values, we test the algorithm for different periodic lengths, L in the z direction. Since we assume periodicity in z direction in any single bubble study, the computational domain should be

appropriately large enough such that any interaction between the bubbles located in each computation cell is a minimum. We have computed the bubble motion by solving the governing equations subject to initial and boundary conditions for $L = 1.5$, $L = 2$, $L = 3$ and up to dimensionless time $t = 100$. These are displayed in the Fig. 6. A total about 3×10^6 time steps are used. The time step, Δt, is chosen to satisfy the stability restriction imposed by inequality (32), and is therefore not a constant for various L. We note, from the Fig. 6, that the description of bubble motion in the Poiseuille flow is influenced by the choice of L. However, the predictions for $L = 2$ and $L = 3$ essentially coincide. On this basis, $L = 3$ is chosen for subsequent computations.

The mesh size and the density ratio in the computations discussed in this paper have been chosen on the basis of computational feasibility. The major computational cost in this study arises from the projection step (step 6 of the algorithm) that is used to solve the variable coefficient Poisson equation (Eq. (35)). We use a multigrid method with a V-cycle for a level projection. All coarse levels are obtained by coarsening the fixed Eulerian grid. The relaxation step consists of two iterations of red-black Gauss–Seidel. Following Almgren et al. [1], the solution on the coarsest level is obtained by using a diagonally preconditioned conjugate gradient routine.

As shown in Fig. 7, as the density ratio, (ρ_2/ρ_1), is decreased toward a more realistic value of 0.001 which would correspond to a gaseous bubble, the CPU units for describing a single bubble motion significantly increase. We note that 10^4 CPU units correspond to 2.8 h on our 2 GHz single processor. In view of this large computational requirement, for subsequent computations, we set the density ratio, (ρ_2/ρ_1), to be 0.1. As illustrated in Fig. 8, the CPU units also significantly increase with an increase in the number of MAC grid points in the r direction, h^{-1}. Again, to compute our results with a reasonable computational effort, we select the mesh size to be $h = 2^{-6}$, in the r and z directions, for subsequent computations.

5.2. Total mass conservation test for the adsorption/desorption scheme of a soluble surfactant

In problems dealing with soluble surfactants, it is very important to conserve the total mass of the soluble surfactant since even a slight trace of surfactant may significantly alter the surface tension, and an error in mass conservation may lead to spurious results. For soluble surfactant transport, at every instant of the

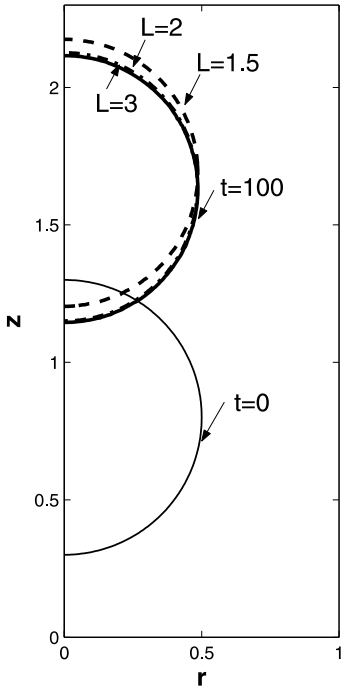

Fig. 6. Optimal computational domain determination for a clean bubble motion in Poiseuille flow, $Re = 10$, $Ca = 0.01$, $t = 100$, solid line is the initial position. ––– $L = 1.5$, -·-·- $L = 2$ and —— $L = 3$.

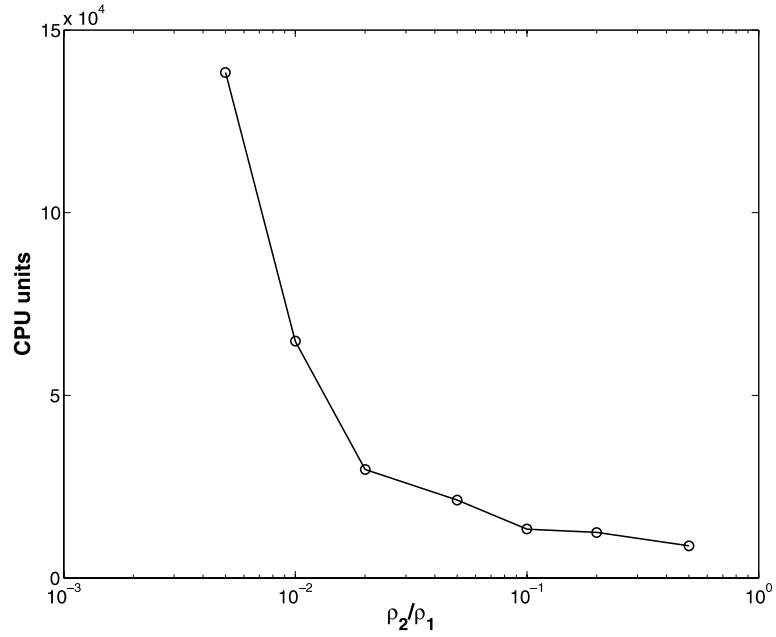

Fig. 7. CPU units for a clean bubble moving in Poiseuille flow for different ρ_2/ρ_1 until $t = 10$, $Re = 10$, $Ca = 0.01$.

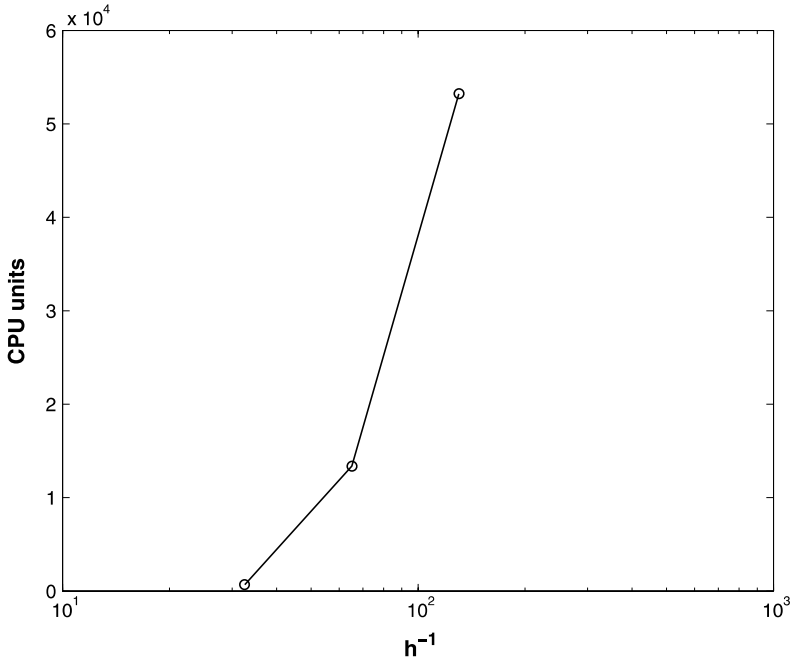

Fig. 8. CPU units for a clean bubble moving in Poiseuille flow for different number of mesh points h^{-1} until $t = 10$, $Re = 10$, $Ca = 0.01$.

process, the amount of surfactant adsorbed on to the interface should be equal to the amount removed from the bulk phase. This feature will be examined here by considering an initially clean bubble in the presence of a soluble surfactant that is initially uniformly distributed in the bulk phase.

For this test, we let the initial bulk concentration, $C_0 = 1 \times 10^{-6}$ mol/cm^3, and take the saturation surface concentration to be, $\Gamma_\infty = 5 \times 10^{-8}$ mol/cm^2, $k_a = 0.1$ cm/s, and $k_d = 0.05$ s^{-1}. We choose a non-dimensional

time that is obtained by dividing the dimensional physical time for the process by the typical time scale governing the adsorption process (r_0/k_a). The quantity, k_a, is the adsorption coefficient. The quantity (r_0/k_a) is much smaller than the bulk diffusion time scale, R^2/D, and we have chosen (r_0/k_a) for non-dimensionalization. The desorption time scale will not be the appropriate one.

As shown in Fig. 9(a) and (b), the soluble surfactant gets transported from the bulk phase onto the interface due to the prevailing concentration gradient. This causes a decrease in the total amount of surfactant in bulk phase. The percentage error in satisfying mass conservation at any instant of the computation is given by the ratio $(M_t - M_e)/M_s \times 100$. This is plotted in Fig. 10 as a function of time. Within a short duration of the process, this error is seen to asymptotically approach 1% of the surface concentration.

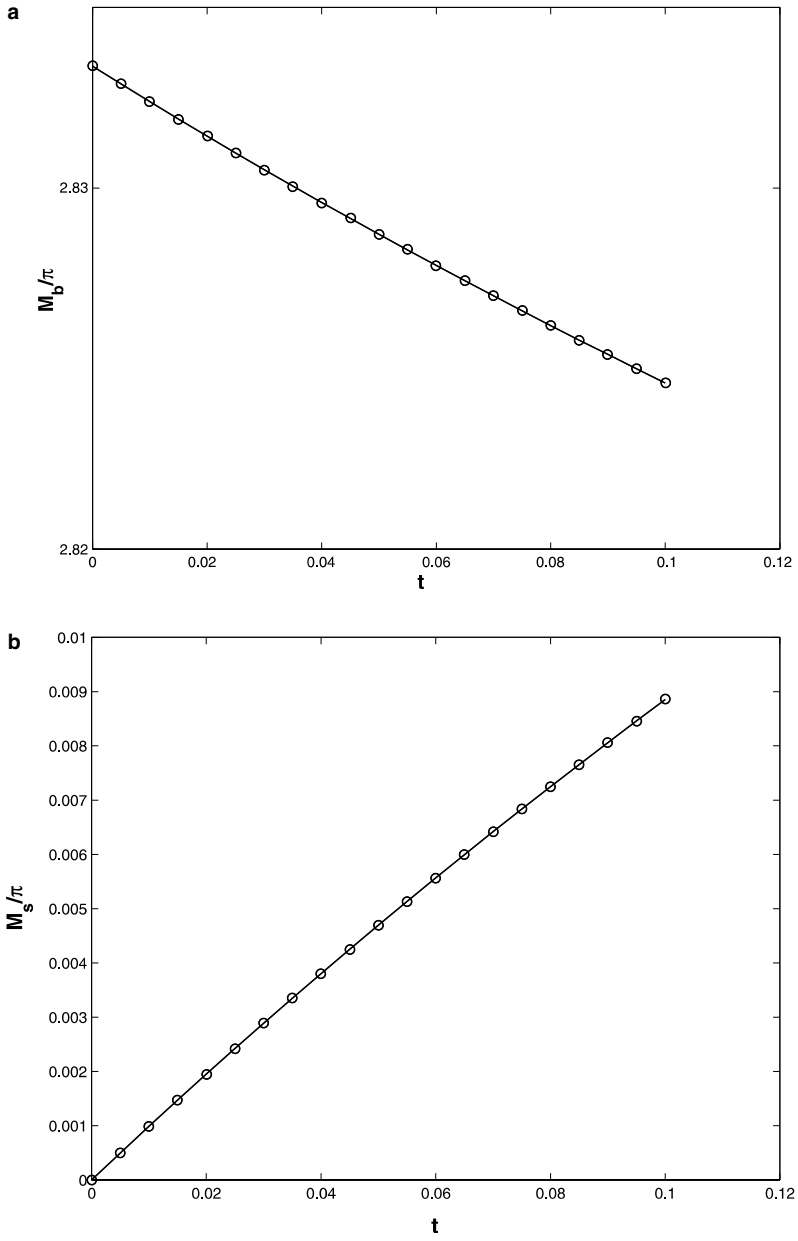

Fig. 9. Mass conservation test for soluble surfactant adsorption onto a clean bubble.

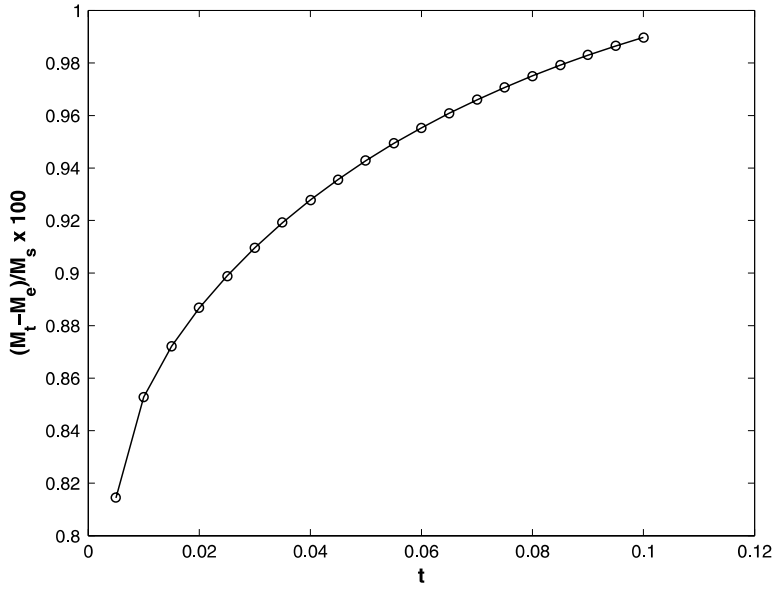

Fig. 10. Percentage error of mass conservation test for soluble surfactant adsorption onto a clean bubble.

5.3. Convergence test of the adsorption/desorption scheme

We consider a static bubble. For given k_a, k_d, number of interfacial grid points, and initial conditions, we vary the size of the fixed background grid and conduct the test to determine the order of convergence. Approach to convergence is implied by a reduction in the predicted change of surface concentration distribution with a change in the grid size. Next, for given k_a, k_d, background grid size, and initial conditions, the size of the interfacial grid is changed to ascertain similar convergence. As illustrated in Fig. 11(a), at given instant of time $t = 0.1$ (small time duration), the solution for the surface concentration, Γ, is seen to converge to a particular form of distribution. Here, the number of interfacial grid points are fixed, $N = 256$. As the mesh size is decreased from 2^{-5} to 2^{-7}, the variations in the prediction of surface concentration appear to decrease. To ascertain the rate of convergence, we plot the logarithm of the L_2 norm of the absolute values of the difference between the solution at the finest level and the solution at the coarser levels as shown in Fig. 11(b). The rate of convergence is found to be second order (slope of the line is 2.0). There is a variation of about one percent from the mean in the predictions of the surface concentration by the algorithm at this instant of time, $t = 0.01$. This variation arises due to the numerical extrapolation of C_S in the integral term of the bulk surfactant transport equation.

Another test for convergence is carried out with a fixed background dimensionless mesh size $h = 2^{-6}$, in both r and z directions. As shown in Fig. 12(a), as the number of the grid points on the interface are increased from 64 to 256, the solution Γ is seen to converge. The rate of convergence is seen to be higher than first order (slope of the line $\sim$1.44) (Fig. 12(b)).

5.4. Surface adsorption/desorption test

To test our adsorption/desorption scheme, first, we consider a clean spherical bubble with a known surface tension of value $\sigma = 1$ dyne/cm immersed in an initially quiescent fluid containing a soluble surfactant, and turn on the surface adsorption scheme. The instantaneous variations of surface concentration Γ along the arc length from $\theta = 0$ to $\theta = \pi$ are plotted in Fig. 13. As expected, since the bubble is stationary, Γ increases with time in an almost uniform fashion along the interface. The magnitude of variation in surface concentration Γ along the interface could be as high as about 2% during early times. This variation, however, decreases with increasing time. Next, we consider a spherical bubble which is initially

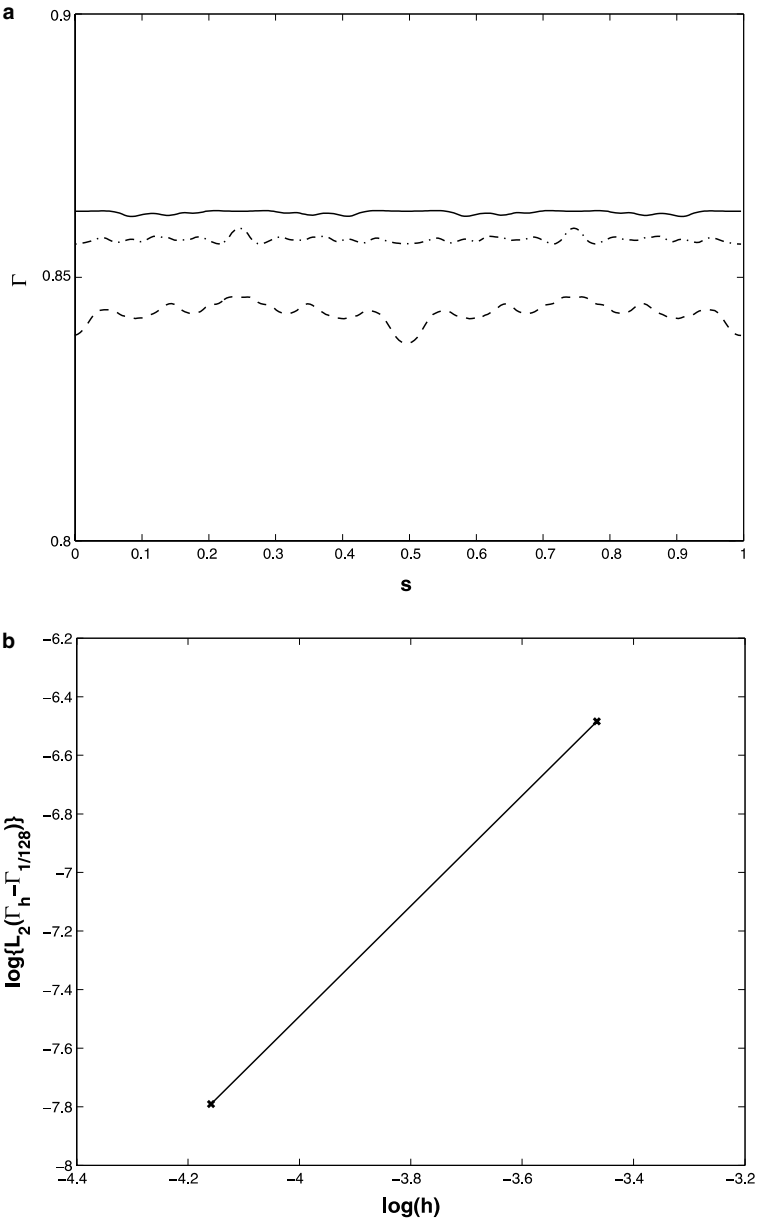

Fig. 11. Convergence test for surface concentration with adsorption for a stationary bubble in a tube. $t = 0.1$s, $N = 256$, $k_a = 0.1$ cm/s, $k_d = 0.05\ s^{-1}$, $C_0 = 1 \times 10^{-6}$ mol/cm^3, $\Gamma_\infty = 2.5 \times 10^{-9}$ mol/cm^2, $D = 1 \times 10^{-3}$ cm^2/s, $D_S = 1 \times 10^{-2}$ cm^2/s. (a) The mesh size: ———, $h = 2^{-5}$; -·-·-, $h = 2^{-6}$; ——, $h = 2^{-7}$. (b) $\log\left\{L_2\left(\left|\Gamma_h - \Gamma_{\frac{1}{128}}\right|\right)\right\}$ as a function of $\log(h)$ for $h = 2^{-5}$, 2^{-6}.

fully covered with the soluble surfactant at a saturated surface concentration, Γ_∞, on the interface. The bubble is immersed in a quiescent fluid containing the surfactant. For this case, k_a is set equal to zero, and only k_d has a non-zero value. The surface concentration Γ uniformly decreases with time. This is shown in Fig. 14.

Fig. 15 displays the equilibrium spatial concentration contours for the surfactant at various locations in the bulk medium away from the bubble interface, at a given instant of time. Because of interfacial adsorption, the soluble surfactant is transported from the bulk phase onto the interface, causing a reduction in bulk concentration as we approach the interface.

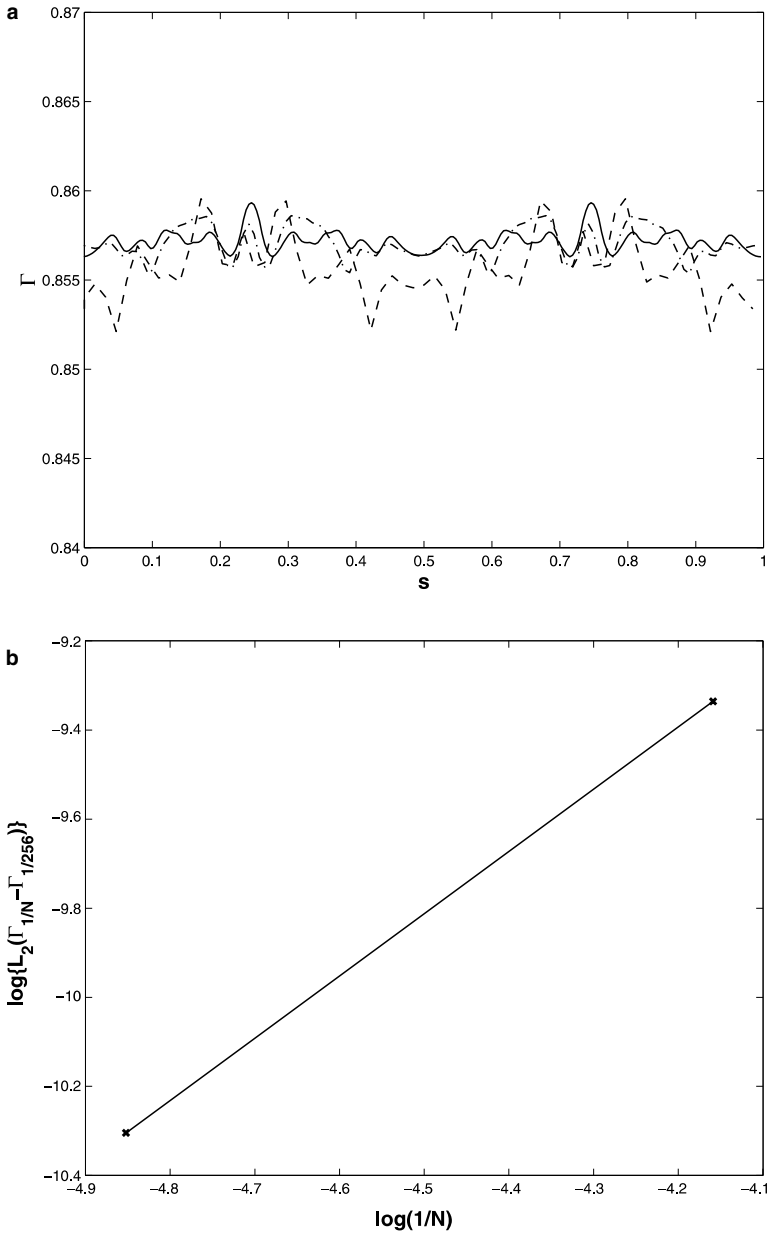

Fig. 12. Convergence test for surface concentration with adsorption for a stationary bubble in a tube. $t = 0.1$s, $h = 2^{-6}$, $k_a = 0.1$ cm/s, $k_d = 0.05\ s^{-1}$, $C_0 = 1 \times 10^{-6}$ mol/cm^3, $\Gamma_\infty = 2.5 \times 10^{-9}$ mol/cm^2, $D = 1 \times 10^{-3}$ cm^2/s, $D_S = 1 \times 10^{-2}$ cm^2/s. (a) The mesh size: ---, $N = 64$, -·-·-; $N = 128$, ——; $N = 256$. (b) $\log\left\{L_2\left(\left|\Gamma_{\frac{1}{N}} - \Gamma_{\frac{1}{256}}\right|\right)\right\}$ as a function of $\log(1/N)$ for $N = 64$, 128.

Next, we consider a bubble with a large dimensionless radius r_0, ($r_0 = 0.9$), and hence a larger volume. In this case, the part of the active interface that is in the vicinity of the equatorial plane of the bubble is closer to the tube wall than the interface locations near the poles. As a result, this configuration will influence the concentration distribution in the bulk medium adjacent to the wall boundary. As illustrated in Fig. 16, when the final adsorption equilibrium is reached, the bulk concentration is non-uniformly distributed in the z direction. A depletion of surfactant concentration is noted to occur adjacent to the tube wall. This feature is similar to what Gaver and co-workers [18] has observed during the steady state motion of a semi-infinite bubble in a solution containing a soluble surfactant.

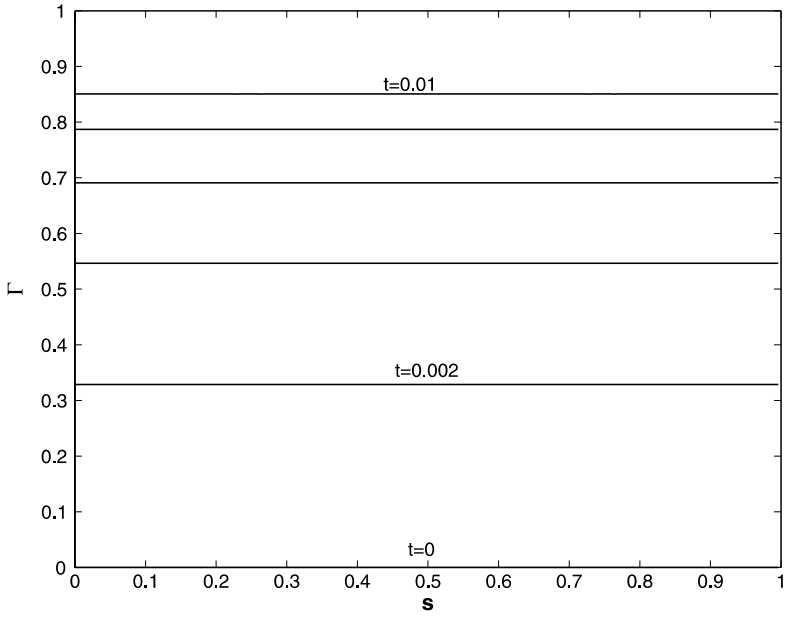

Fig. 13. Surface concentration along the interface for adsorption on a stationary bubble in a tube. $r_0 = 0.5$, $k_a = 1$ cm/s, $k_d = 10\ s^{-1}$, $C_0 = 1 \times 10^{-6}$ mol/cm^3, $\Gamma_\infty = 2.5 \times 10^{-9}$ mol/cm^2, $D = 1 \times 10^{-3}$ cm^2/s, $D_S = 1 \times 10^{-2}$ cm^2/s for $t = 0$, 0.002, 0.004, 0.006, 0.008, 0.01.

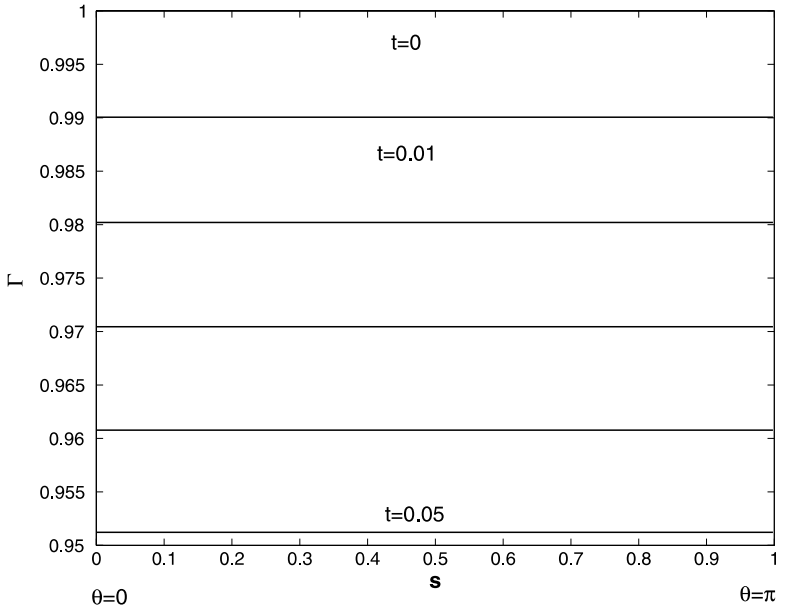

Fig. 14. Surface concentration along the interface for adsorption on a stationary bubble in a tube. $r_0 = 0.5$, $k_a = 0$ cm/s, $k_d = 10\ s^{-1}$, $C_0 = 1 \times 10^{-6}$ mol/cm^3, $\Gamma_\infty = 2.5 \times 10^{-9}$ mol/cm^2, $D = 1 \times 10^{-3}$ cm^2/s, $D_S = 1 \times 10^{-2}$ cm^2/s for $t = 0$, 0.01, 0.02, 0.03, 0.04, 0.05.

5.5. Langmuir model vs. Frumkin model

Because of the existence of different macromolecules in blood and diverse behaviors of surfactant adsorption/desorption, various models, such as Langmuir and Frumkin models, have been used to explain the observed complicated behaviors [7]. In the previous calculations, Langmuir isotherm is assumed for the adsorption model. However, the flexibility of our code enables extension to describe other adsorption isotherms. To illustrate this feature, we now adopt a Frumkin isotherm given by

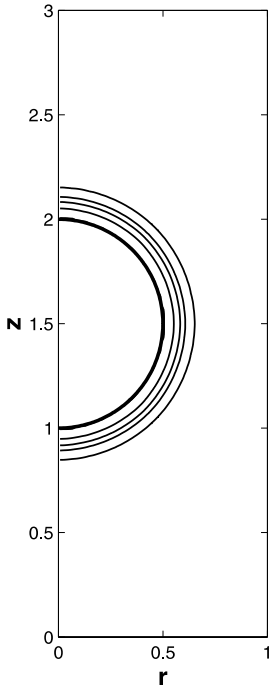

Fig. 15. Adsorption of an initially clean bubble in a tube. Bulk concentration contour at $t = 2$, $C = 0.65$ (innermost contour), 0.8, 0.9, 0.95, 0.99 (outermost contour). $r_0 = 0.5$.

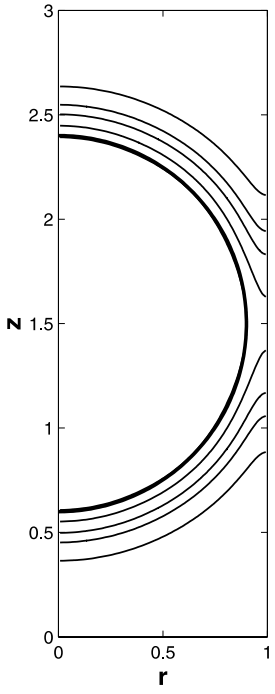

Fig. 16. Adsorption of a initially clean bubble with larger volume in a tube. Bulk concentration contour at $t = 2$, $C = 0.65$ (innermost contour), 0.8, 0.9, 0.95, 0.99 (outermost contour). $r_0 = 0.9$.

$$\frac{\mathrm{d}\Gamma(t)}{\mathrm{d}t} = k_\mathrm{a} C_\mathrm{s}\left(1 - \frac{\Gamma}{\Gamma_\infty}\right) - k_\mathrm{d}\Gamma \exp\left(-A\left(\frac{\Gamma}{\Gamma_\infty}\right)\right). \tag{62}$$

Here, we choose $A = 2$, $k_\mathrm{a} = 0.1$, and $k_\mathrm{d} = 50$.

As shown in Fig. 17, for a static bubble, we note that the Langmuir and Frumkin adsorption models drive the surface concentration toward different equilibrium surface concentration values. These are 1.4703×10^{-9} and 1.9796×10^{-9} mol/cm^2, for the two isotherms, respectively. The difference between the two isotherms is in the desorption term, and the usage of any specific isotherm is of significance when k_d is large enough. This could potentially impact on the description of the dynamic behavior of the bubble.

5.6. Surface diffusion test

Here, we test the algorithm for a stationary spherical bubble with only the surface diffusion scheme turned on. There are 256 grid points along the interface. The time step needs to satisfy the stability requirement

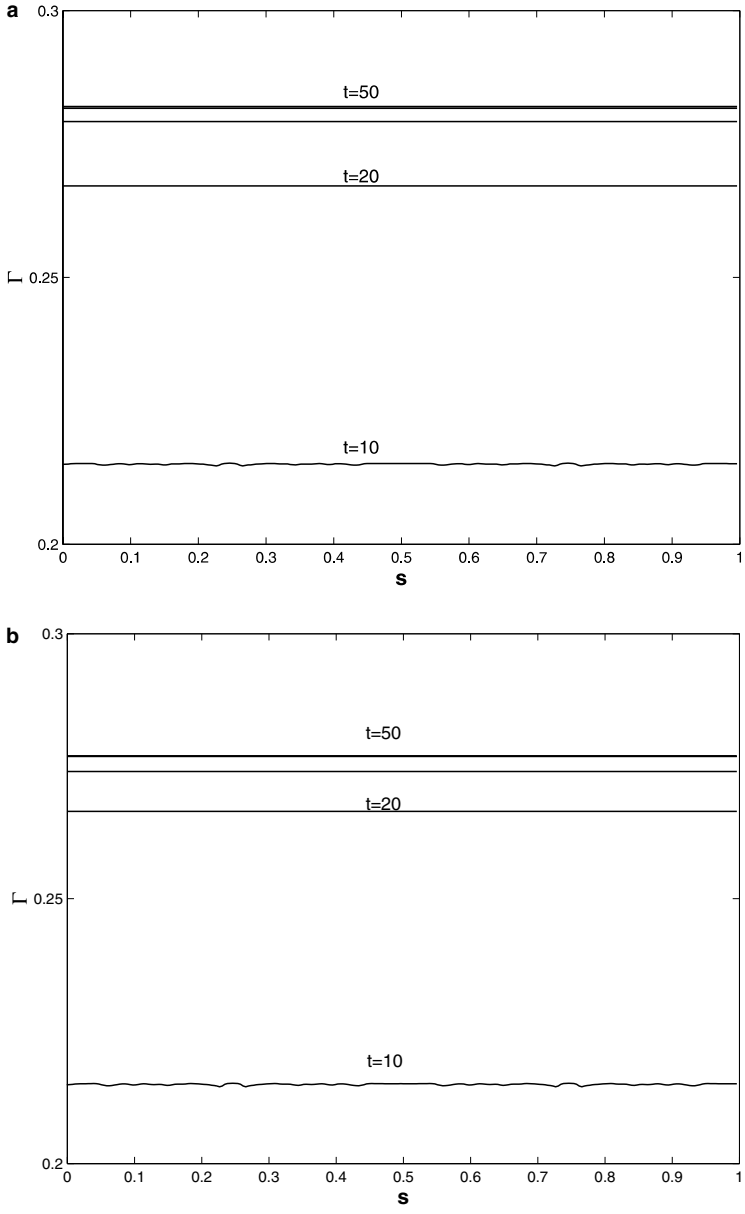

Fig. 17. Adsorption of a initially clean bubble. Surface concentration contours at $t = 10$, 20, 30, 40 and 50 s. (a) Langmuir model (b) Frumkin model.

$$\Delta t \leqslant \frac{2h^2}{Pe_s}. \tag{63}$$

On this basis, Δt is chosen as 2×10^{-6} for $Pe_s = 10$. Initially, there is a prescribed variation in the distribution of the surface concentration, $\Gamma_0 = (1 - \cos(\theta))/2$. As shown in Fig. 18, the surface diffusion process acts to even out the initially non-uniform distribution of the surfactant. An exact solution for this variation has been given by James and Lowengrub [20] as

$$\Gamma(\theta, t) = \frac{1}{2}\left[1 - \exp\left(\frac{-2t}{Pe_s R^2}\right)\cos\theta\right]. \tag{64}$$

Our numerical prediction agrees well with the exact solution in this case.

5.7. Test for the Marangoni effect

To test for the Marangoni effect, we consider a bubble that is initially covered with a non-uniformly distributed surface concentration Γ given by, $\Gamma = \Gamma_0 * (1 + \tanh(4(\theta/\pi - 0.5)))$. Initially, bubble and the bulk medium are both quiescent. We let, $\rho_1 = 1$, $\rho_2 = 0.1$ and $\mu_1 = 0.1$, $\mu_2 = 0.01$ for this test. Since there is a variation of surface concentration along the interface, and the surface tension, $\sigma(\Gamma)$, depends on surface concentration Γ as given by Eq. (26), the Marangoni effect will initiate a propulsion of the bubble. This causes the bubble to move away from its initial position, as shown in Fig. 19(a). The Marangoni number is defined as $Ma = E/Ca$, where E is the elasticity number, and Ca is the Capillary number. For this test, this number is small. However, Marangoni effect still exists. As the surface concentration evolves, the shape of the bubble undergoes slight changes and this is illustrated in Fig. 19(b). The velocity field of the bubble and its surrounding fluid at $t = 5$ is shown in Fig. 20(a). It is interesting to note the evolution of Γ along the interface in Fig. 20(b). Since there is more surfactant at the bottom portion of the bubble, ($\theta = 0$), than toward the top, ($\theta = \pi$), a gradient is created and this causes a Marangoni flow along the interface. The flow along the interface advects the surfactant toward the top of the bubble. This results in a lowering of the concentration at the bottom ($\theta = 0$). At a later time, $t = 5$, the maximum surface concentration is located almost midway between the top and bottom ($\theta \approx \pi/2$).

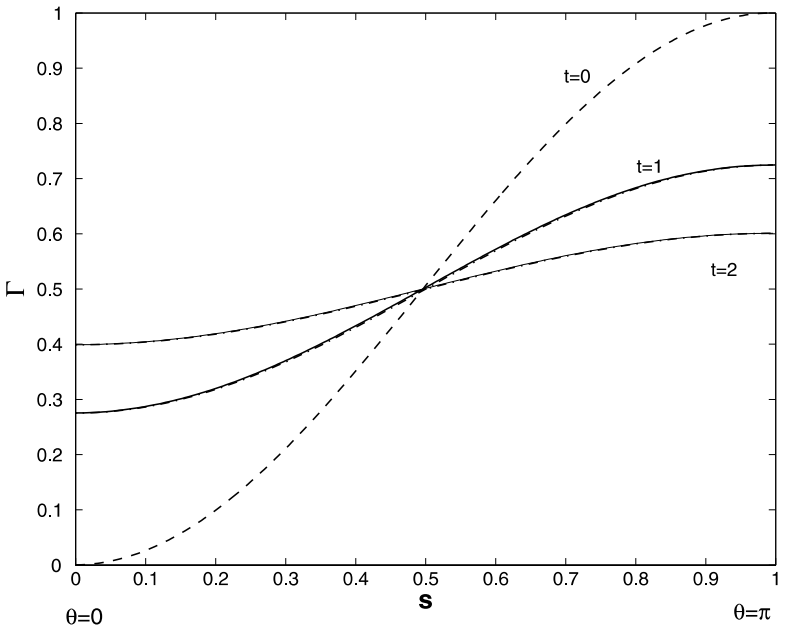

Fig. 18. Surface diffusion test for surface concentration of surfactant Γ on a stationary bubble in a tube. $Pe_s = 10$, -·-·-; exact solution, —— numerical solution.

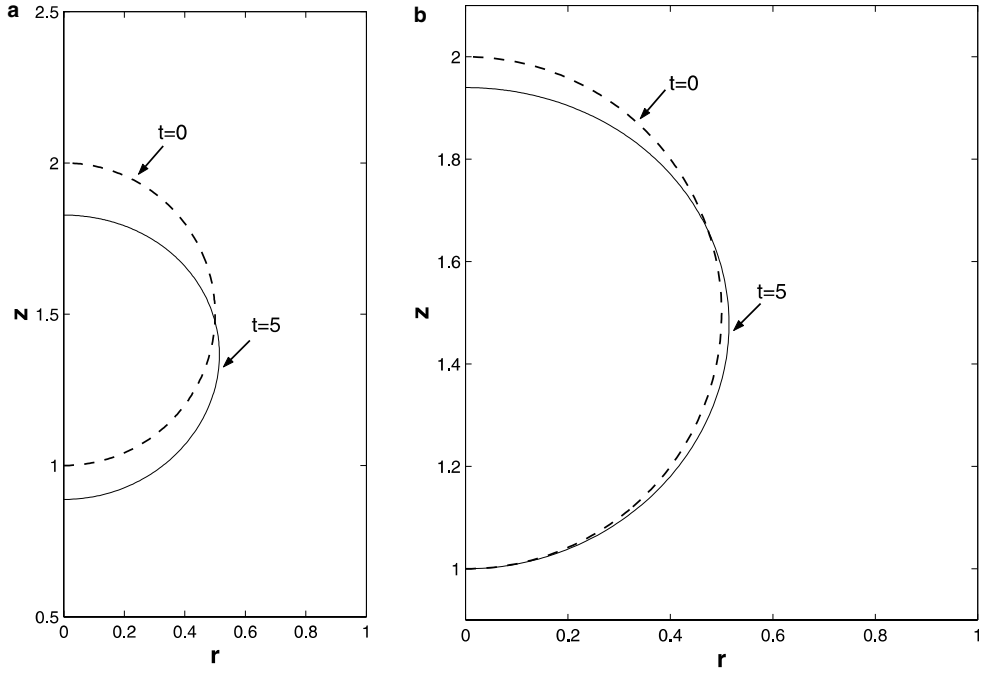

Fig. 19. Marangoni effects for an initially non-uniform surfactant covered bubble in a tube. (a) Bubble locations at $t = 0$, 5, (b) bubble shapes at $t = 0$, 5 (shifted back to the initial location).

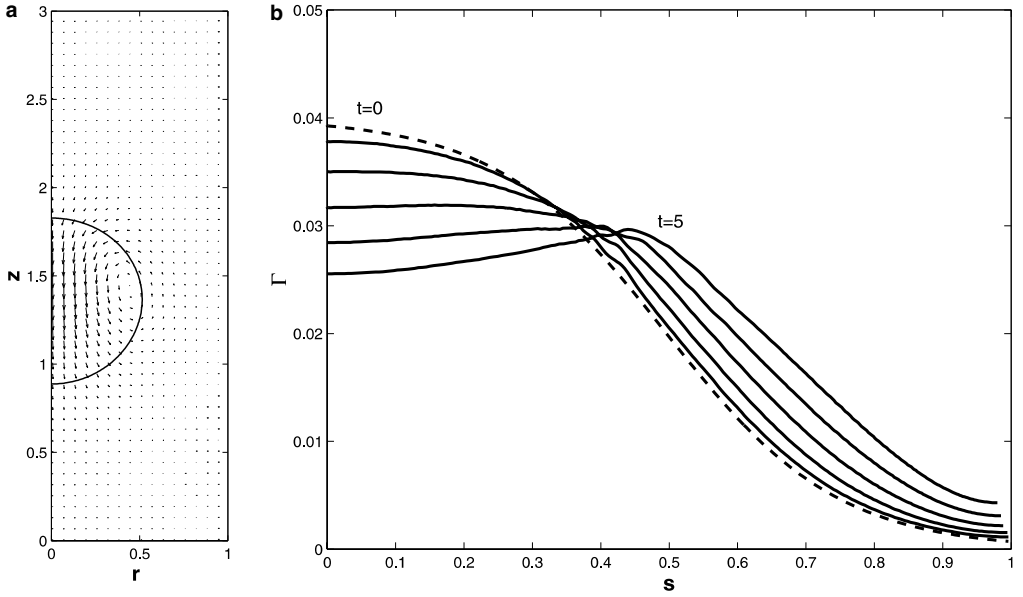

Fig. 20. Marangoni effects for an initially non-uniform surfactant covered bubble in a tube. (a) Streamline in the reference frame of bubble at $t = 5$, (b) surface concentration Γ at $t = 0$, 1, 2, 3, 4, 5.

5.8. Surfactant coated bubble in Poiseuille flow

Next, we numerically simulate the motion of a bubble covered with an insoluble surfactant and in Poiseuille flow, and compare the motion with that of a clean bubble in a surfactant free environment, also in Poiseuille

flow. The dimensionless parameters are $Re = 1$, and $Ca = 0.01$. For the insoluble surfactant, since there is no adsorption or desorption, $St_a = St_d = 0.0$, and for the contaminated bubble, we initially assume a uniform distribution of surface concentration, Γ, of the insoluble surfactant. As shown in Fig. 21(a), the contaminated bubble also moves in the direction of the flow but at a lower rate of speed compared to that of the clean bubble. Because of the surface convection, the surfactant moves along the interface causing a build up of surface concentration at the rear part of the interface (near $\theta = 0$), as shown in Fig. 21(b). The surface tension is

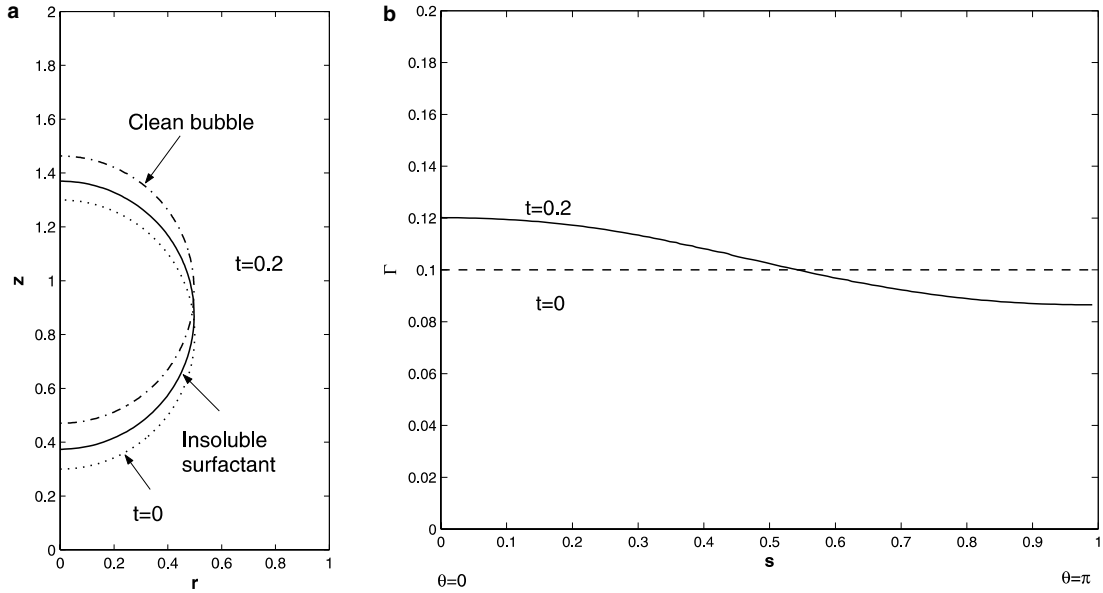

Fig. 21. Motion of an initially uniformly covered bubble in Poiseuille flow in the presence of insoluble surfactant. $Re = 1$, $Ca = 0.01$, $Pe = 100$, $Pe_s = 100$, $St_a = 0$, $St_d = 0$, $\lambda = 0.01$.

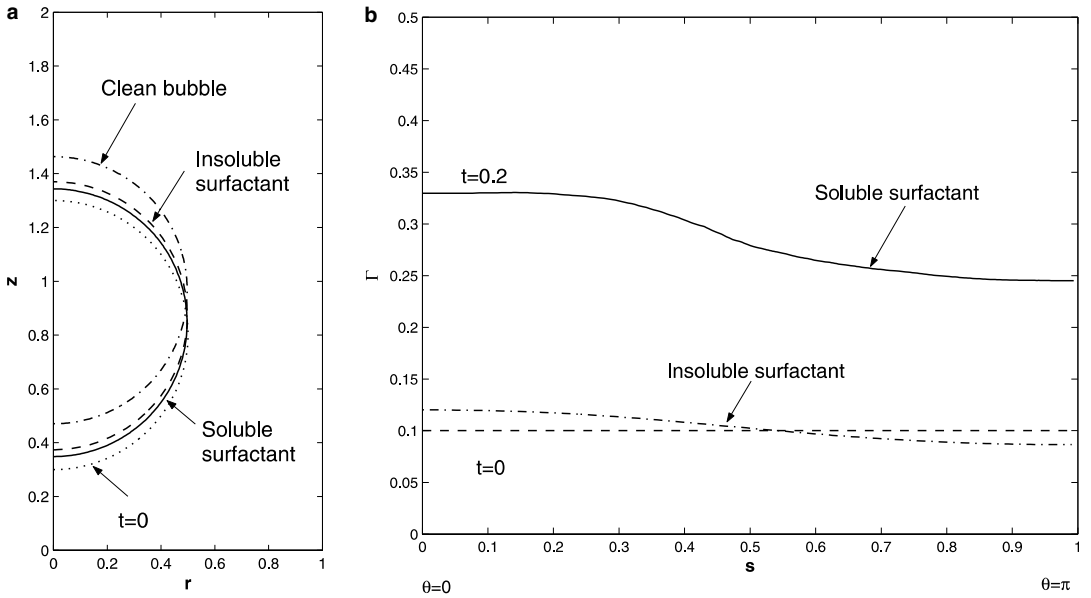

Fig. 22. Motion of an initially uniformly covered bubble in Poiseuille flow in the presence of soluble surfactant. $Re = 1$, $Ca = 0.01$, $Pe = 100$, $Pe_s = 100$, $St_a = 0.1$, $St_d = 0.05$, $\lambda = 0.01$.

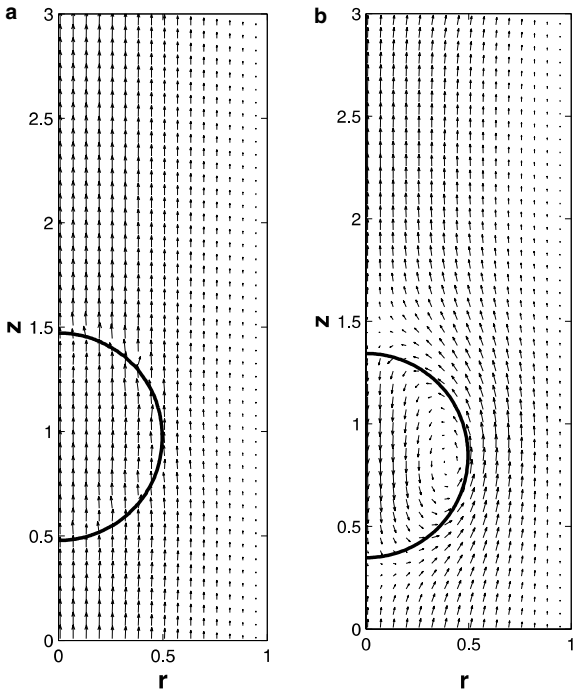

Fig. 23. Velocity for a bubble (a) without surfactant, (b) with soluble surfactant. $Re = 1$, $Ca = 0.01$, $Pe = 100$, $Pe_s = 100$, $St_a = 0.1$, $St_d = 0.05$, $\lambda = 0.01$.

reduced at the rear while it is increased in the front portion. This gives rise to Marangoni effect causing a surface tension gradient driven motion in a direction opposite to that of the primary flow. The net result is a slowing down of the contaminated bubble motion. Equivalently, since the presence of the surfactant increases the drag on the bubble, the contaminated bubble moves at a reduced speed.

Next, we consider a bubble in Poiseuille flow but now in the presence of a soluble surfactant. The adsorption/desorption scheme is turned on. With $Re = 1$, and, $Ca = 0.01$, the bubble is initially covered with a uniform distribution of a soluble surfactant. This initial surface concentration volume is set to be the same as that for the insoluble surfactant case studied earlier. Since the chosen initial surface concentration is below its equilibrium value, surfactant is adsorbed onto the interface from the bulk phase. At a given instant of time, as seen in Fig. 22(b), the total surface amount for the soluble surfactant case happens to be larger than that for the corresponding insoluble surfactant case. This results in an increased reduction of the surface tension at the front of the bubble, resulting in a stronger Marangoni effect. As a consequence, the bubble in the presence of the soluble surfactant is noted to move even slower than a bubble in the presence of an insoluble surfactant (Fig. 22(a)).

As shown in Fig. 23, there is a fundamental difference between the velocity field for a clean bubble and a contaminated one in a pressure driven flow. A clean bubble travels with the bulk fluid. However, a contaminated bubble's motion is retarded by the circulation induced by the surface gradient of the surfactant.

6. Conclusion

Based on a front tracking scheme, a comprehensive algorithm has been developed for studying the axisymmetric motion of a deformable bubble contained in a tube and in the presence of a soluble/insoluble surfactant. The major interest here is on the dynamic adsorption of the soluble surfactant which nonlinearly alters the surface tension, and this in turns affects the flow and transport in a complicated way. Also, since a bubble–liquid interface is being examined, there is a need to accommodate a concentration jump across the interface in the evaluation of flow and transport. The adsorption scheme for the soluble

surfactant is carefully designed such that the total mass of the surfactant is well conserved and mass flux is accurately resolved by using an interface indicator function. This represents an advance in treating problems of this class. Tests on the efficacy of various aspects of the algorithm have been carried out. These include tests for the convergence of the adsorption scheme, for the adsorption/desorption scheme, for surface diffusion, for the Marangoni effect, and the combined effects of an imposed Poiseuille flow and Marangoni flow. The algorithm has the flexibility of studying different models for adsorption and surfactant surface tension models, such as the Langmuir and Frumkin models. These models have significant practical relevance. The numerical results are qualitatively consistent with analytical results where available. The results presented include an example of Marangoni flow which causes a bubble to propel out of its initial static location due to the development of a surface tension gradient. It is also shown that the bubble motion in Poiseuille flow may be significantly slowed down due to the presence of a soluble surfactant in the bulk medium. For identical initial surface concentrations of the surfactant, the bubble motion is more retarded in the presence of a soluble surfactant compared to that of an insoluble surfactant. In that case, the Marangoni induced motion is in a direction opposite to that driven by the bulk pressure. Our study indicates that as the location of the adsorptive interface gets closer to the tube wall, the bulk fluid in the vicinity of the interface may become depleted of surfactant, an observation that has particular significance in understanding gas embolism and for developing therapeutic measures. Further detailed study is needed to clarify this observation.

Our motivation for this algorithm is to provide a platform for computing intravascular multiphase flow where complicated interfacial mechanisms are at play. Further implementation of the adaptive mesh capability of the present algorithm is expected to provide a significant benefit for studies of the gas embolism problem and the associated surfactant treatment issues. This study has shown that computational costs become prohibitively large with dimensionless mesh size approaching 2^{-7} and the density ratio $\rho_2/\rho_1 \sim 0.001$. This points to the need for Supercomputer facilities for investigating realistic parameter ranges that have direct value for applications in health sciences.

Acknowledgments

We gratefully acknowledge NIH Grant RO1 HL 67986-01 A1 for supporting this study. We also thank Professors A.S. Almgren, D.D. Joseph, A. James, Dr. K. Mukundakrishnan and Mr. Josh Lampe for their kind help and insightful discussions.

Appendix A

In one dimension, suppose liquid phase presents in the interval $x > 0$.

$$\delta_{2,h}(x) = \begin{cases} \frac{2}{h}\left(1 - \frac{x}{h}\right), & 0 \leqslant x < h, \\ 0, & \text{otherwise.} \end{cases} \tag{65}$$

Then, denoting the interval $[0,h)$ as I_k, we have

$$\langle \delta_{2,h}(x), \phi \rangle = \int_{I_k} \delta_{2,h}(x)\phi(x)\,\mathrm{d}x = \phi(0) + \int_{I_k} \delta_{2,h}(x)(\phi(x) - \phi(0))\,\mathrm{d}x \tag{66}$$

and

$$\left| \int_{I_k} \delta_{2,h}(x)(\phi(x) - \phi(0))\,\mathrm{d}x \right| \leqslant \int_{I_k} \delta_{2,h}(x)|\phi(x) - \phi(0)|\,\mathrm{d}x \leqslant \max|\phi(x) - \phi(0)| \tag{67}$$

If ϕ is continuous at $x = 0$, the maximum tends to 0 as $h \to 0$. Therefore

$$\lim_{h \to 0} < \delta_{2,h}(x), \phi >= \phi(0) \tag{68}$$

for every ϕ continuous at origin, and $\delta_{2,h}(x)$ distributionally converges to delta function.

References

[1] A.S. Almgren, J.B. Bell, P. Colella, L.H. Howell, M.L. Welcome, A conservative adaptive projection method for the variable density incompressible Navier–Stokes equations, J. Comput. Phys. 142 (1998) 1–46.
[2] A.B. Branger, D.M. Eckmann, Accelerated arteriolar gas embolism reabsorption by an exogenous surfactant, Anesthesiology 96 (4) (2002) 971–979.
[3] B. Bunner, G. Tryggvason, Dynamics of homogeneous bubbly flows. Part 1. Rise velocity and microstructure of the bubbles, J. Fluid Mech. 466 (2002) 17–52.
[4] B. Bunner, G. Tryggvason, Dynamics of homogeneous bubbly flows. Part 2. Rise velocity fluctuations, J. Fluid Mech. 466 (2002) 53–84.
[5] D.P. Cavanagh, D.M. Eckmann, Interfacial dynamics of stationary gas bubbles in flows in inclined tubes, J. Fluid Mech. 398 (1999) 225–244.
[6] H.D. Ceniceros, The effects of surfactants on the deformation and evolution of capillary waves, Phys. Fluids 15 (2003) 245–256.
[7] C.H. Chang, E.I. Franses, Adsorption dynamics of surfactants at air/water interface: a critical review of mathematical models, data and mechanism, Colloid Surface A100 (1995) 1–45.
[8] R.P. Chhabra, Encyclopedia Fluid Mech. 7 (1988) 253–286.
[9] R.P. Chhabra, Bubbles, Drops and Particles in Non-Newtonian fluids, CRC Press, Boca Raton, FL, 1993.
[10] B. Cuenot, J. Magnaudet, B. Spennato, The effects of slightly soluble surfactants on the flow around a spherical bubble, J. Fluid Mech. 339 (1997) 25–53.
[11] D. De Kee, R.P. Chhabra, Transport Processes in Bubbles, Drops and Particles, Taylor and Francis Group, 1992.
[12] D. De Kee, C.F. Chan Man Fong, J. Yao, Bubble shape in non-Newtonian fluids, J. Appl. Mech. 69 (5) (2002) 703–704.
[13] M.A. Drumright-Clarke, Y. Renardy, The effects of insoluble surfactant at dilute concentration on drop breakup under shear with inertia, Phys. Fluids 16 (2004) 14–21.
[14] D.M. Eckmann, V.N. Lomivorotov, Microvascular gas embolization clearance following perfluorocarbon administration, J. Appl. Physiol. 94 (2003) 860–868.
[15] C.D. Eggleton, Y.P. Pawar, K.J. Stebe, Insoluble surfactant on a drop in an extension flow: a generalization of the stagnated surface limit to deforming interfaces, J. Fluid Mech. 385 (1999) 79–99.
[16] C.D. Eggleton, T.M. Tsai, K.J. Stebe, Tip streaming from a drop in the presence of surfactants, Phys. Rev. Lett. 87 (4) (2001). Art. No. 048302.
[17] S.N. Ghadiali, D.P. Gaver, The influence of non-equilibrium surfactant dynamics on the flow of a semi-infinite bubble in a rigid cylindrical capillary tube, J. Fluid Mech. 478 (2003) 165–196.
[18] S.N. Ghadiali, D. Halpern, D.P. Gaver, A dual-reciprocity boundary element method for evaluating bulk convective transport of surfactant in free-surface flows, J. Comput. Phys. 171 (2001) 534–559.
[19] F. Gibou, R. Fedkiw, L.T. Cheng, M. Kang, A second order accurate symmetric discretization of the Poisson equation on irregular domains, J. Comput. Phys. 176 (2002) 205–227.
[20] A. James, J. Lowengrub, A surfactant-conserving volume-of-fluid method for interfacial flows with insoluble surfactant, J. Comput. Phys. 201 (2004) 685–722.
[21] Y.J. Jan, G. Tryggvason, Computational studies of contaminated bubbles, in: I. Sahin, G. Tryggvason (Eds.), Proceedings of a Symposium on the Dynamics of Bubbles and Vorticities near a Free Surface, AMD, vol. 119, ASME, 1991, pp. 46–59.
[22] D. Juric, G. Tryggvason, A front-tracking method for dendritic solidification, J. Comput. Phys. 123 (1996) 127–148.
[23] D. Juric, G. Tryggvason, Computations of boiling flows, Int. J. Multiphase Flow 24 (1998) 387–410.
[24] D.M. Leppinen, M. Renksizbulut, R.J. Haywood, The effects of surfactants on droplet behavior at intermediate Reynolds numbers I. The numerical model and steady state results, Chem. Eng. Sci. 51 (3) (1996) 479–489.
[25] X.F. Li, C. Pozrikidis, The effect of surfactant on drop deformation and on the rheology of dilute emulsion in Stokes flow, J. Fluid Mech. 341 (1997) 165–194.
[26] X.J. Li, Z.S. Mao, The effect of surfactant on the motion of a buoyancy-driven drop at intermediate Reynolds number: a numerical approach, J. Colloid Interf. Sci. 240 (2001) 307–322.
[27] Y. Liao, J.B. McLaughlin, Bubble motion in aqueous surfactant solutions, J. Colloid Interf. Sci. 224 (2000) 297–310.
[28] W.J. Milliken, L.G. Leal, The influence of surfactant on the deformation and breakup of a viscous drop, J. Colloid Interf. Sci. 166 (1994) 275–285.
[29] M.L. Minion, On the stability of Godunov-projection methods for incompressible flow, J. Comput. Phys. 123 (1996) 435–449.
[30] H.N. Oğuz, S.S. Sadhal, Effects of soluble and insoluble surfactants on the motion of drops, J. Fluid Mech. 194 (1988) 563–579.
[31] C.W. Park, Influence of soluble surfactant on the motion of a finite bubble in a capillary tube, Phys. Fluids A 4 (11) (1992) 2335–2347.
[32] C.S. Peskin, Numerical analysis of blood flow in the heart, J. Comput. Phys. 25 (1977) 220–252.
[33] Y.Y. Renardy, M. Renardy, V. Cristini, A new volume-of-fluid formulation for surfactants and simulations of drop deformation under shear at a low viscosity ratio, Eur. J. Mech. B 21 (2002) 49–59.
[34] D. Rodrigue, Generalized correlation for bubble motion, Am. Inst. Chem. Eng. 47 (2001) 39–44.
[35] D. Rodrigue, A simple correlation for gas bubbles rising in power-law fluids, Can. J. Chem. Eng. 80 (2002) 289–292.
[36] D. Rodrigue, D. De Kee, C.F. Chan Man Fong, The slow motion of a single gas bubble in a non-Newtonian fluid containing surfactants, J. Non-Newtonian Fluid Mech. 86 (1999) 211–227.
[37] S.S. Sadhal, P.S. Ayyaswamy, J.N. Chung, Transport Phenomena with Drops and Bubbles, Springer, New York, 1997.

[38] H.A. Stone, A simple derivation of the time dependent convection diffusion equation for surfactant transport along a deforming interface, Phys. Fluids A 2 (1990) 111–112.
[39] M. Sussman, E.G. Puckett, A coupled level set and volume-of-fluid method for computing 3D and axisymmetric incompressible two-phase flows, J. Comput. Phys. 162 (2000) 301–337.
[40] M. Sussman, A second order coupled level set set and volume-of-fluid method for computing growth and collapse of vapor bubbles, J. Comput. Phys. 187 (2003) 110–136.
[41] F. Takemura, Adsorption of surfactants onto the surface of a spherical rising bubble and its effect on the terminal velocity of the bubble, Phys. Fluids 17 (2005) 048104.
[42] T.M. Tsai, M.J. Miksis, Dynamics of a drop in a constricted capillary tube, J. Fluid Mech. 274 (1994) 197–217.
[43] T.M. Tsai, M.J. Miksis, The effects of surfactant on the dynamics of bubble snap-off, J. Fluid Mech. 337 (1997) 381–410.
[44] G. Tryggvason, B. Bunner, A. Esmaeeli, D. Juric, N. Al-Rawahi, W. Tauber, J. Han, S. Nas, Y.J. Jan, A front-tracking method for the computations of multiphase flow, J. Comput. Phys. 169 (2001) 708–759.
[45] S.O. Unverdi, G. Tryggvason, Computations of multi-fluid flows, Physica D 60 (1992) 70–83.
[46] C.E. Weatherburn, Differential Geometry of Three Dimensions, vol. I, Cambridge University Press, Cambridge, UK, 1927.
[47] J.J. Xu, H.K. Zhao, An Eulerian formulation for solving partial differential equations along a moving interface, J. Sci. Comp. 19 (2003) 573–594.
[48] S. Yon, C. Pozrikidis, A finite volume/boundary-element method for flow past interfaces in the presence of surfactants, with application to shear flow past a viscous drop, Comput. Fluids 27 (1998) 879–902.
[49] H. Zhou, V. Cristini, J. Lowengrub, C.W. Macosko, 3D adaptive finite element simulations of deformable drops with soluble surfactant: pair interactions and coalescence, Phys. Fluids (submitted).